



H2020-ICT-25-2016-2017



HYbrid FLying rollIng with-snakeE-aRm robot for contact inSpection

HYFLIERS

D5.3

Results of the preliminary testing of the integrated system

Contractual date of delivery	31 Jul 2022
Actual date of delivery	7 Oct 2022
Editor(s)	P.J. Sanchez-Cuevas (CATEC)
Author(s)	R. Schmid (GEIR), V. Lippiello (CREATE), J. Cacace (CREATE) Guillermo Heredia (USE), Ulrico Celentano, Miika Sikala, Juha Rönning (UOULU)
Workpackage	WP5
Estimated person-months	42
Dissemination level	PU
Type	R
Version	1.0
Total number of pages	53

Abstract:

This document presents the results of the preliminary testing of the integrated hybrid robots. Those results analyse the performance of the robots under controller scenarios indoors and outdoors. The deliverable shows results of the different components of the integrated robots and shows how the system performs during a full mission.

Keywords:

Hybrid robot. Aerial robot. Satellite robot. Magnetic attractor. Hyper-redundant robotic arm. UT inspection. Miniature UT probe. Pipe inspection. Remote inspection. Refinery. Operations support. Ground station. Emergency behaviour.

Executive summary

This document presents the results of the preliminary testing of the integrated hybrid robots. Those results analyse the performance of the robots under controller scenarios indoors and outdoors. The deliverable shows results of the different components of the integrated robots and shows how the system performs during a full mission.

The document summarized several results that evidence that the technology developed in the context of the HYFLIERS project is promising and targets an actual problem. The technology readiness level (TRL) achieved of the different components and different robots has allowed us to test an integrated version of them in controlled scenarios. It is important to remark that according to the proposal, the Hybrid Mobile Robot (HMR) aims to be positioned with a TRL 6, however, some parts of the HMR system will reach higher TRLs. This will be the case of the inspection satellite mounted in the flying platform. In contract, the Hybrid Robot with Arm (HRA) aims to push the state-of-the-art a little bit more through innovative and original concepts. As a consequence, HRA developments target a TRL 5.

The results collected in this deliverable (D5.3) in combination with the D5.1 and D5.2, show that both robot and their different subsystems were successfully tested through several experiments in controlled scenarios, and they are ready to start the validation phase along with the WP6.

Abbreviations and symbols

API	Application Programming Interface
CAN	Controller Area Network
CATEC	Centro Avanzado de Tecnología Aeroespaciales
CMD	Command prompt
CoM	Centre of Mass
CREATE	Consorzio C.R.E.A.T.E.
CRUD	Create, Read, Update, Delete
DB	Database
DBUS	Desktop Bus
DC	Direct Current
DN	Diameter Nominal
DoF	Degree of Freedom
EC	European Commission
ETH	Ethernet
ESC	Electronic Speed Controller
FPV	First Person View
FRR	Full Requirement Robot
FuMo	Functional Model
GEIR	GE Inspection Robotics
GPS	Global Positioning System
HD	High Definition
HDMI	High Definition Multimedia Interface
HLC	High Level Computer
HYFLIERS	Hybrid flying rolling with-snake-arm robot for contact inspection
HMR	Hybrid Mobile Robot
HR	Hybrid Robot
HRA	Hybrid Robot w/ Arm
HTTP	Hypertext Transfer Protocol
ICT	Information and communications technology
IMU	Inertial Measurement Unit
GCS	Ground Control Station
JSON	JavaScript Object Notation
LCD	Liquid Crystal Display
LiPo	Lithium-Polymer
LRR	Limited Requirement Robot
PC	Personal Computer
PID	Proportional-Integral-Derivative
PPM	Pulse-Position Modulation
PVC	PolyVinyl Chloride
PWM	Pulse Width Modulation

REST	Representational state transfer
RGB	Red Green Blue
ROS	Robot Operating System
RPA	Remotely Piloted Aircraft
SAP	Snake Arm with pan and tilt Probe
TRL	Technology Readiness Level
TX	Transmitter
UAV	Unmanned Aerial Vehicle
UI	User Interface
UOULU	University of Oulu
USB	Universal Serial Bus
USE	Universidad de Sevilla
UT	Ultrasound Transducer
VMC	Visual Meteorological Conditions
WP	Workpackage

Table of Contents

Executive summary.....	2
Abbreviations and symbols.....	3
1. Introduction.....	10
2. HMR experiments.....	11
2.1. Pose estimator	11
2.2. Pipe detector.....	14
2.3. PID-Control and state machine	15
2.3.1. Take-off state	15
2.3.2. Find pipe state	16
2.3.3. Orientation state	16
2.3.4. Landing on pipe state	17
2.4. Crawler.....	18
2.4.1. Measurement.....	18
2.4.2. Calibration.....	19
2.4.3. Navigation.....	19
2.4.4. Line following horizontal pipe 12 and 6 o'clock.....	20
2.4.5. Line following horizontal pipe 3 and 9 o'clock.....	20
2.4.6. Line following horizontal elbow 3 and 9 o'clock.....	21
2.4.1. Line following horizontal elbow 12 and 6 o'clock.....	21
2.4.2. Weld crossing.....	22
2.4.3. Surface coating.....	22
2.5. UT results.....	23
2.5.1. Calibration block.....	23
2.5.2. Straight pipe	29
2.5.3. Elbow	30
2.6. Inspection data processing	31
2.6.1. Inspection plan	31
2.6.1. Straight pipe	32
2.6.2. Elbow	34
2.6.3. Inspection report	35
2.7. Full experiments.....	36
3. HRA experiments.....	39
3.1. Testing of the HRA rolling landing gear add-on.	39
3.2. Testing of the HRA with the crawler clamp landing gear add-on.	42

3.3. Arm

3.4. Full experiment

4. Conclusions.....

References.....

43

50

52

53

List of figures

Figure 1 HMR final architecture.	11
Figure 2 Left: Comparison of the position in the squared trajectory; Right: Comparison of the position in the pipe approach trajectory.	12
Figure 3 APE evaluation in squared trajectory.	12
Figure 4 Relative orientation error in the squared trajectory.	13
Figure 5 Distance error from estimated pose to cylinder axis in the two experiments.	14
Figure 6 Full mission control results.	15
Figure 7 Take-off state control results.	15
Figure 8 Find pipe state control results.	16
Figure 9 Orientation state control results.	16
Figure 10 Landing on pipe state control results.	17
Figure 11: Circumferential raster.	18
Figure 12: Longitudinal raster.	18
Figure 13: Calibration mockup.	19
Figure 14: Crawler positioning relative to weld.	19
Figure 15: Camera view and references.	20
Figure 16: Horizontal 8" pipe line scan at 12 o'clock.	20
Figure 17: Horizontal 8" pipeline scan at 3 o'clock.	21
Figure 18: Crawler path along the outside of an elbow.	21
Figure 19: Path along the top of the elbow.	21
Figure 20: Weld crossing tested.	22
Figure 21: Surface coating test.	22
Figure 22: UT calibration S1.	23
Figure 23: UT calibration S2.	24
Figure 24: UT calibration S3.	24
Figure 25: UT calibration S4.	25
Figure 26: UT calibration S5.	25
Figure 27: UT calibration S6.	26
Figure 28: UT calibration S7.	26
Figure 29: UT calibration S8.	27
Figure 30: UT calibration S9.	27
Figure 31: UT calibration S10.	28
Figure 32: UT straight pipe inspection results.	29
Figure 33: UT elbow inspection results.	30
Figure 34: The GSDB UI.	31
Figure 35: Inspection plan for the preliminary validation tests.	31
Figure 36: GSDB subsystem waiting data from the UT subsystem.	32
Figure 37: GSDB subsystem receiving data from the UT subsystem.	32
Figure 38: Straight pipe inspection results are collected at the inspection report.	33
Figure 39: Straight pipe inspection results: 12 o'clock (360°) and 6 o'clock (180°) positions.	33
Figure 40: Straight pipe inspection results: 3 o'clock (90°) and 9 o'clock (270°) positions.	34
Figure 41: Also elbow inspection results are now collected at the inspection report.	34
Figure 42: Elbow inspection results: 12 o'clock (360°) and 6 o'clock (180°) positions.	35
Figure 43: Elbow inspection results: 3 o'clock (90°) and 9 o'clock (270°) positions.	35

Figure 44: The inspection report for the preliminary validation tests as visualised on the support tool.	36
Figure 45: HMR takes off and looks for the pipe.	36
Figure 46: HMR during orientation and landing phases.	37
Figure 47: HMR landed on pipe.	37
Figure 48: HMR satellite moving over the pipe.	38
Figure 49: HMR takes off and returns home.	38
Figure 50 HRA software architecture.	39
Figure 51 Outdoor validation scenario with two arrays of pipes.	40
Figure 52 Sequence of images showing the experiment.	40
Figure 53 Reference path and execution of the path by the HRA.	41
Figure 54 Evolution of the multirotor position and orientation during the experiment.	41
Figure 55 Experiment with HRA with crawler clamp.	42
Figure 56 Pitch and roll attitude angles of the HRA with crawler clamp during the experiment.	43
Figure 57: Prototype of the hybrid aerial-ground mobile manipulator for thickness inspection.	43
Figure 58: Prototype of the hybrid aerial-ground mobile manipulator for thickness inspection.	44
Figure 59: Laboratory mock-up with two adjacent pipes.	45
Figure 60: Pipe inspection procedure: rotation in clockwise direction, initial position, rotation in counter-clockwise direction.	45
Figure 61: Elbow position during a longitudinal motion of the end-effector. The position of the mobile base over the pipe is commanded to maintain the elbow joint closer to the body of the platform. From top to bottom, the position of the end-effector in the longitudinal direction, the error of the elbow with respect to the desired angle and the position of the rover along the pipe. In blue the same data without the projection onto the null space (the curves in blue are the upper curve in the mid subfigure and the lower curve in the bottom subfigure).	46
Figure 62: Compensation around the pitch axis during the motion of the arm, thanks to the battery sliding mechanism. From top to bottom, the Cartesian position of the end-effector, the position of the battery, the estimated wrench around the y axis (pitch). In blue the same data without the projection onto the null space.	47
Figure 63: Lateral inspection of an 8 inches pipe with EMAT sensors, in a laboratory mock-up.	47
Figure 64: Time histories of joint position commands to bring the tool on the inspection point.	48
Figure 65: Measured roll angle of the platform on the pipe (top) and the estimated torque around the x axis of the pipe during the motion of the arm (bottom) without the external force compensation.	48
Figure 66: Measured and commanded roll angle of the platform on the pipe (top) and the estimated torque around the x axis of the pipe during the motion of the arm (bottom) with external force compensation.	49
Figure 67: The damaged pipe used to test the inspection capabilities.	49
Figure 68: B-Scan graphic generated after the inspection. The rectangle marks the corroded section.	50
Figure 69: Sequence of images of one of the experiments in the HYFLIERS outdoors mock-up scenario.	51

List of tables

Table 1 Results for squared trajectory 13

Table 2 Results for pipe approach trajectory 13

Table 3 Mean errors for pipe post estimation 14

1. Introduction

This deliverable outlines the results of the preliminary testing of the hybrid robots developed in the HYFLIERS project. It is important to remark that according to both the previous deliverables and the project proposal, the consortium has developed two different robotic systems in the context of HYFLIERS project. Those systems are targeting different inspection scenarios and have been developed with different technology readiness levels (TRL).

The two approaches can be summarized as follows:

- **Hybrid Mobile Robot (HMR):** This hybrid robot can take-off, fly, land and move on a pipe to perform the inspection required by the end-users. This system is focused on the magnetic pipes inspection, and it is composed of an aerial vehicle adapted to the industrial environment and a satellite vehicle with the capability of crawling along the pipe to carry out the pipe inspection with the sensors mounted on-board.
- **Hybrid Robot with Arm (HRA):** The HRA is focused on magnetic and non-magnetic pipe inspection using a lightweight robotic arm with an ultrasound transducer (UT) probe. The system will be able to land on magnetic and non-magnetic isolated pipes and pipe racks. It consists of a modular aerial platform and different add-ons which will be used depending on the application. Due to HRA is targeting a wider range of application and more challenging scenarios (magnetic and non-magnetic pipes and pipe racks), this prototype is expected to have a lower TRL. Instead, it is expected to generate a greater scientific impact driven by a more significant innovation.

The Hybrid Mobile Robot (HMR) aims to be positioned with a TRL 6, however, some parts of the HMR system will reach higher TRLs. This will be the case of the inspection satellite mounted in the flying platform. In contrast, the Hybrid Robot with Arm (HRA) aims to push the state-of-the-art a little bit more through innovative and original concepts. As a consequence, HRA developments target a TRL 5.

As it was mentioned above, the rest of the document describes in detail the preliminary tests accomplished with both robots before their proper validation along with the WP6. These tests have been done at the level of the unitary subsystems and complete systems to evaluate the performance of each solution in controlled scenario. The authors of this deliverable strongly recommend the readers to follow this document, the D5.1 and the D5.2, together to completely understand the HYFLIERS system.

2. HMR experiments

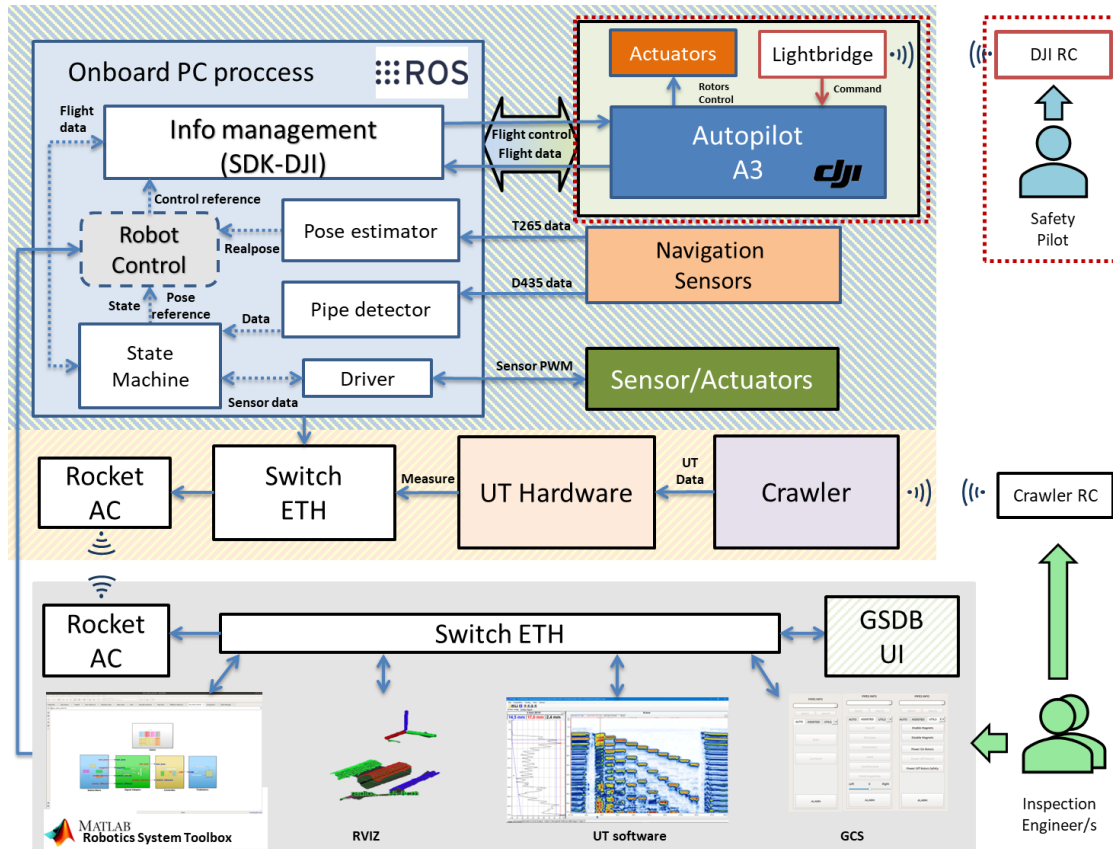


Figure 1 HMR final architecture.

According to the HMR final architecture presented in the D5.2 (see Figure 1) the key components developed in the context of the projects that takes part during the HMR operation are the pose estimator, the pipe detector, the robot control or proportional-integral-derivative (PID) controller with the state machine, the robotic satellite (called in this deliverable robotic crawler) and the UT system. These deliverable analyses the performance of each component in the integrated robot during their specific test. It also shows the HMR during a complete operation along the Section 2.6. This deliverable is related to the results presented in the D5.1 and D5.2, we highly recommend following this document together with D5.1 and D5.2.

2.1. Pose estimator

This subsection shows the results obtained with the Redundant Kalman Filter. Two types of experiments have been repeatedly tested in our VICON facility to evaluate filter performance: a squared trajectory, and the execution of the complete mission, i.e. from take-off to pre-landing on the pipe (instead of actually landing), return to the take-off location and land. We have used evo package [1] to align different sources of odometry and calculate the absolute pose error (APE). This metric evaluates the global consistency of the estimated trajectory by comparing the absolute distances between the estimations and the ground truth provided by the VICON motion capture system. Moreover, the estimated orientation is also evaluated through the relative orientation error, even though this value is not part of our state vector. The motivation of this plot is assessed if the orientation estimation provided by the onboard autopilot is accurate enough for the purposes of our application. Figure 2, Figure 3 and Figure 4 show the results of those experiments.

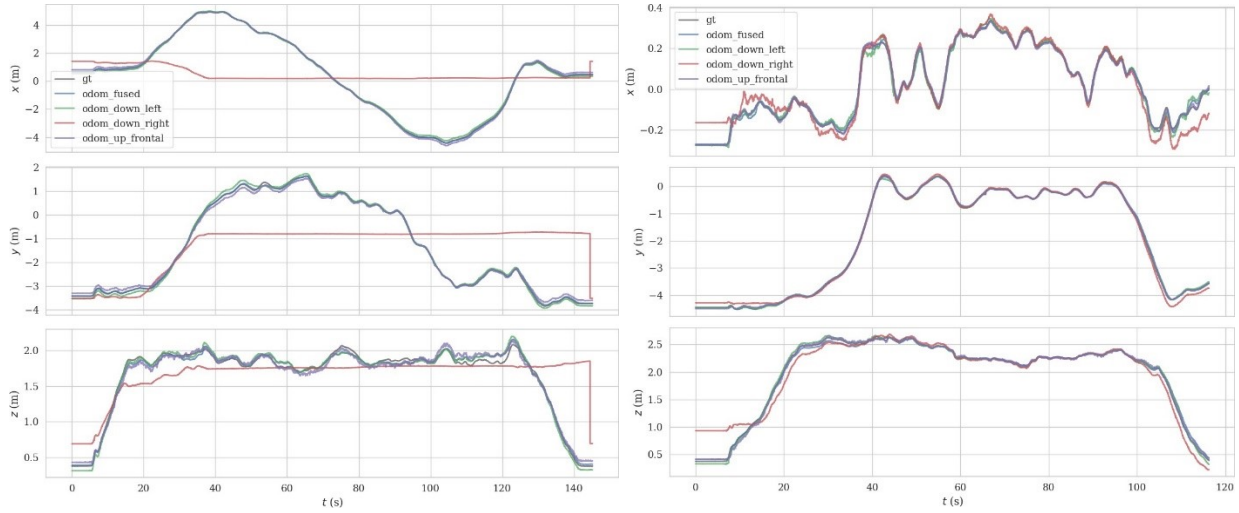


Figure 2 Left: Comparison of the position in the squared trajectory; Right: Comparison of the position in the pipe approach trajectory.

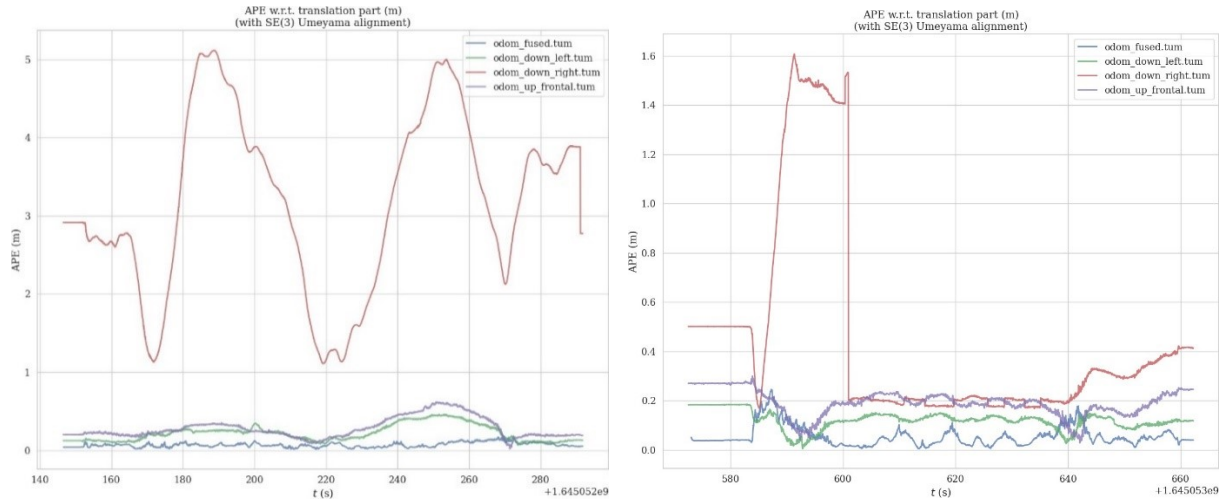


Figure 3 APE evaluation in squared trajectory.

Squared Trajectory Evaluation: During this experiment, one of the sensors failed. This was due to some external problem associated with the odometry of the lower-right camera on the aircraft. Figure 2 shows the trajectory performed during the experiment.

Figure 3 shows the APE of each odometry source and the result of the sensor fusion. It can be seen how the proposed localization improves the estimations obtained by each sensor individually, and how it is able to avoid the effect of the failure of one of the sensors. This can be also seen in Table 1, where several metrics for each sensor and our fused approach are shown.

These results demonstrate the correct functioning of the proposed sensor fusion strategy. Even if there is an error in an odometry source, due to the redundant sensor system, it is possible to continue navigating autonomously through the inspection area.

Table 1 Results for squared trajectory

	DownRight	DownLeft	UpFrontal	Ours
RMSE	3.3810	0.2459	0.3127	0.0744
Mean	3.1873	0.2221	0.2840	0.0684
Median	3.2201	0.2052	0.2360	0.0633
Std	1.1280	0.1055	0.1309	0.0292
Min	1.1111	0.0646	0.0226	0.0137
Max	5.1173	0.4600	0.6183	0.1807
Sse	81151.2	429.555	694.438	39.3058

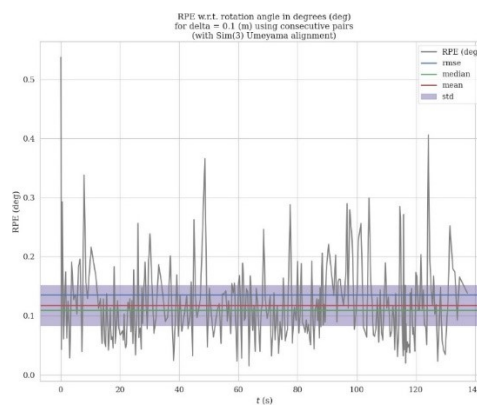
Pipe Approach Trajectory Evaluation: During the development of this experiment, a trajectory similar to the one that is performed in the autonomous mission has been carried out. Thus, it is possible to evaluate if the proposed filter improves the results for the use case. Table 2 shows the trajectory performed during this experiment.

In contrast to the previous experiment, none of the tracking cameras completely failed. Instead, there was a temporal failure for a fraction of time at the beginning, but the odometry later recovered. Even so, the estimated localization was still better than that obtained by the odometry sources individually. Table 3 shows the APE in this trajectory, and Table 2 covers the main metrics for each sensor and our fused approach.

Table 2 Results for pipe approach trajectory

	DownRight	DownLeft	UpFrontal	Ours
RMSE	0.6275	0.1263	0.1983	0.0660
Mean	0.4651	0.1207	0.1910	0.0533
Median	0.2996	0.1202	0.1906	0.0412
Std	0.4212	0.0371	0.0533	0.0388
Min	0.1676	0.0047	0.0282	0.0047
Max	1.6072	0.1854	0.3136	0.2453
Sse	1650.21	66.8622	164.799	18.1259

Orientation evaluation: Figure 4 shows the relative orientation error between the estimated pose and the ground-truth. As it can be seen, the mean error is around 0.12 degrees, showing that the orientation used, which comes directly from the autopilot, is sufficiently accurate for performing safe autonomous missions.

**Figure 4** Relative orientation error in the squared trajectory.

It has been shown that the proposed solution obtains sufficiently good results when no sensor fails, and when the input odometry sources exhibits some drift. This would allow the inspection mission to be performed autonomously and safely.

2.2. Pipe detector

The pipe detection has been evaluated with two experiments on the same use case. From these, the average error in the pipeline estimation has been calculated. It should be noted that these flights have been carried out in manual mode, to also decouple the integration of the VICON localization with the control strategy, which could bring oscillations to the platform. During the execution of an autonomous mission, this error is more stable since the flight of the aircraft is more stable as well. Figure 5 shows the evolution of the estimated distance error over time for these experiments.

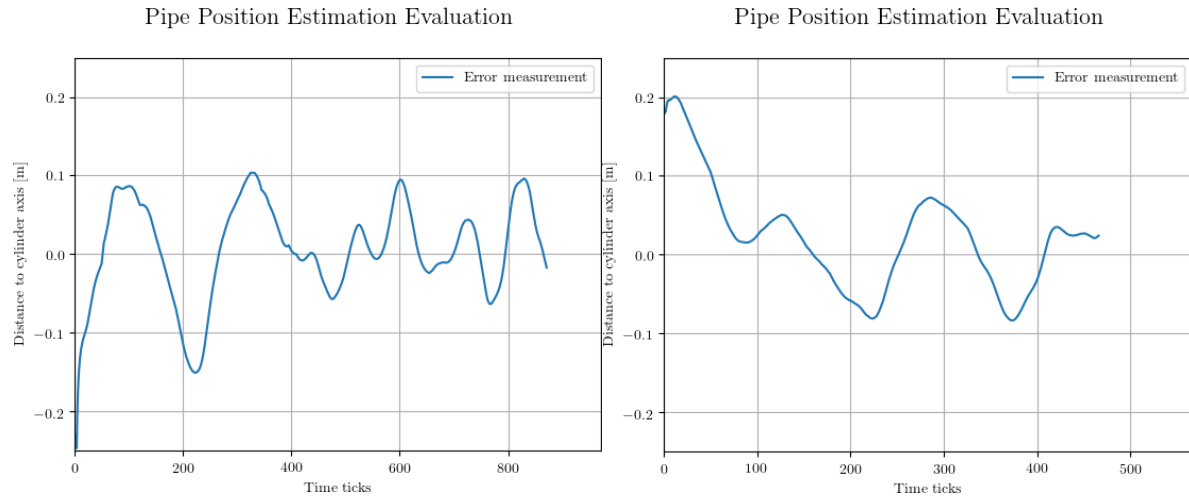


Figure 5 Distance error from estimated pose to cylinder axis in the two experiments.

The average error in the estimation of the pipe position is less than 5cm, as Table 3 shows. This allows asserting that in cylinders whose radius is larger, it will be possible to land the aircraft and perform autonomous inspections.

When performing an autonomous flight, the position of the aircraft is more stable. This will allow to maintain low estimation errors over time and feedback to the controllers necessary to land autonomously on the pipe.

Table 3 Mean errors for pipe post estimation

	Experiment 1	Experiment 2
Mean Error	0.0495	0.0439

2.3. PID-Control and state machine

This section shows the results of the HMR PID-controller implemented to manage the high-level actions of the robot. Figure 6 shows the performance of the robot during different states of the state machine in an actual mission. Following figures are focusing on assessing the performance of the HMR in its specific flight modes. Figure 6 shows that the hybrid robot is able to follow the control reference while flying during a complete operation. All the results show the capability of the robot of tracking x, y, z and yaw, because those are the controllers developed for the HMR. The attitude control is directly accomplished by the DJI A3 autopilot.

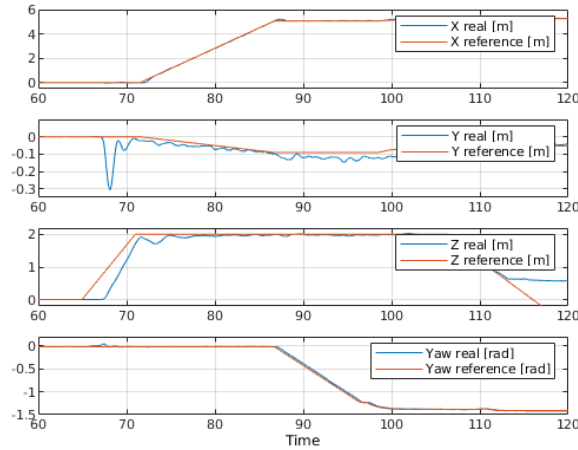


Figure 6 Full mission control results.

2.3.1. Take-off state

This section shows the results of the autonomous take-off manoeuvre implemented in the HMR. Figure 7 illustrates the capability of the robot to reach the desired height and maintains the stability starting the flight from the ground.

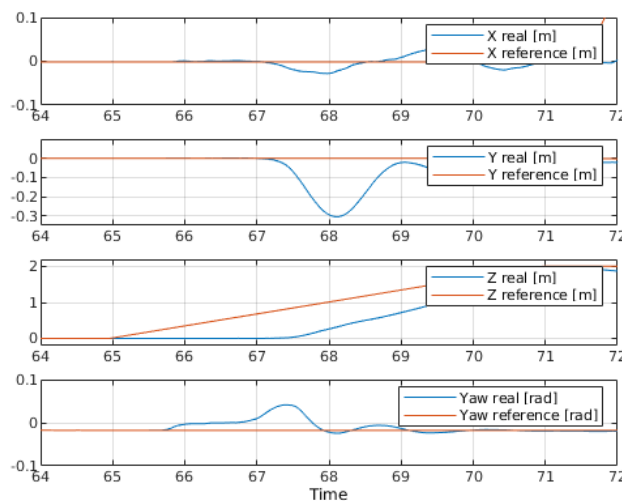


Figure 7 Take-off state control results.

2.3.2. Find pipe state

Figure 8 shows the movement that the robot does when it is in the find pipe mode and its capability to follow the desired trajectory. These results show that the robot is perfectly able to follow a trajectory with a constant speed and it is also showing the reference commanded by the state machine in the find pipe state.

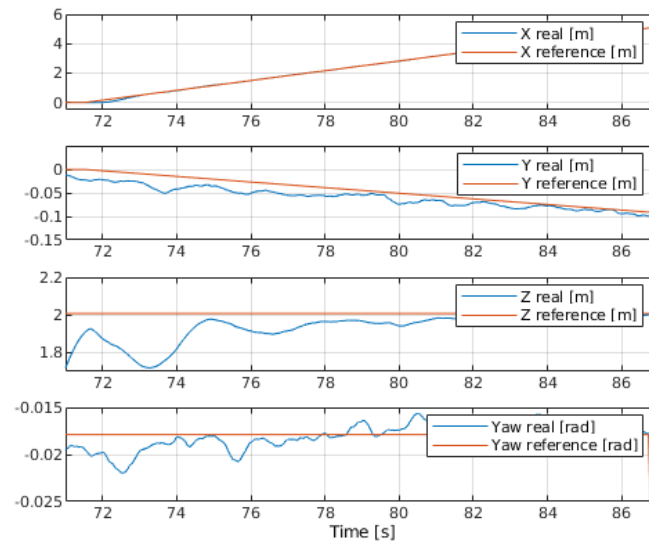


Figure 8 Find pipe state control results.

2.3.3. Orientation state

Figure 9 shows the robot flying in the orientation state. In this state the robot should align itself with the detected pipe. The robot maintains a static height while moving in the horizontal plane and aligning its yaw with the pipe direction. The controller is able to track the commanded reference without significant errors.

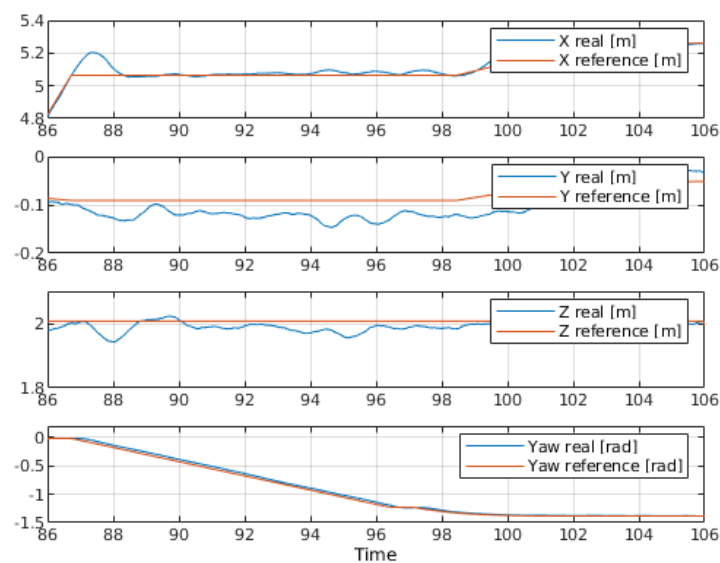


Figure 9 Orientation state control results.

2.3.4. Landing on pipe state

The landing on pipe state generates the descent trajectory towards the pipe and of maintaining the horizontal position and orientation with respect to the pipe calculated in the "Orientation" state. This state also has control over the modification of the horizontal position, since the software designed to estimate the position of the pipe remains in operating. The results of Figure 10 show the tracking errors of the controller while accomplishing this operation. These results show the capability of the robot of safely executing the landing on pipe state manoeuvre.

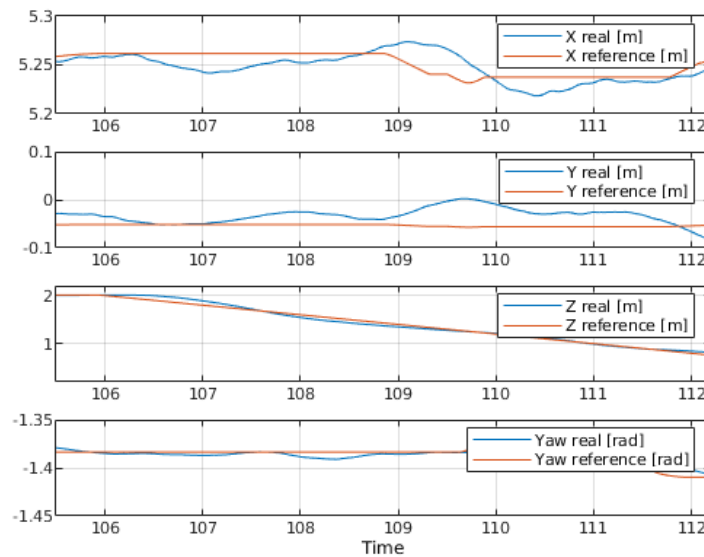


Figure 10 Landing on pipe state control results.

2.4. Crawler

2.4.1. Measurement

The requirements in D1.1 outline the need for point measurements on straight pipes and elbows as a Must requirement and T-pieces and reducers as Should or Could requirements. The targeted locations are close to the welds to adjoining piping elements in the four quadrant locations 3, 6, 9 and 12 o'clock. For that purpose, it must be possible to position the crawler to an accuracy of 20 mm (UR-34) in longitudinal direction from the weld and in circumferential direction in respect to the quadrant locations.

Additionally, the system Must be able to perform grid inspections on straight pipes and elbows. Should and Could for T-pieces and reducers. For these more advanced inspection techniques it is important to consider how the satellite would be moved to gather the required inspection data. These tests have shown that a most stable signal for the wall thickness measurement is achieved when the crawler is oriented in longitudinal direct to the pipe. This is due to the suspension of the drive units being under additional load, increasing contact force on the central probe. Circumferential movements however are subject to more variation on the contact force primarily from the weight of the satellite reducing the contact force too much when at the underside of the pipe.

Grid measurements based on multiple spaced circumferential line scans as drafted in Figure 11 were therefore judged to be infeasible for these small pipe diameters.

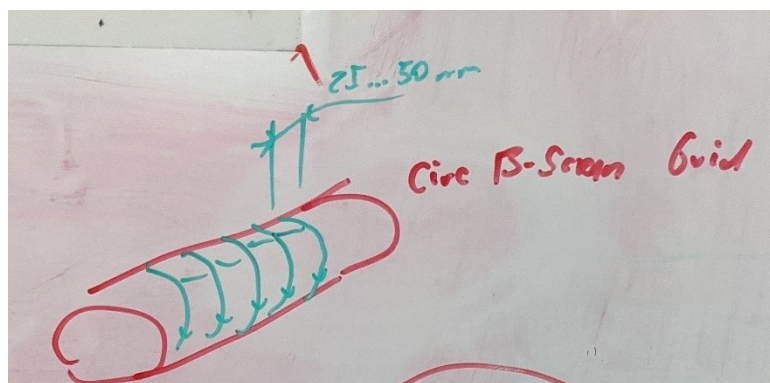


Figure 11: Circumferential raster.

Instead, the longitudinal line scans of Figure 12 along the four quadrant orientations around the pipe would be followed to test the more advanced inspection techniques.

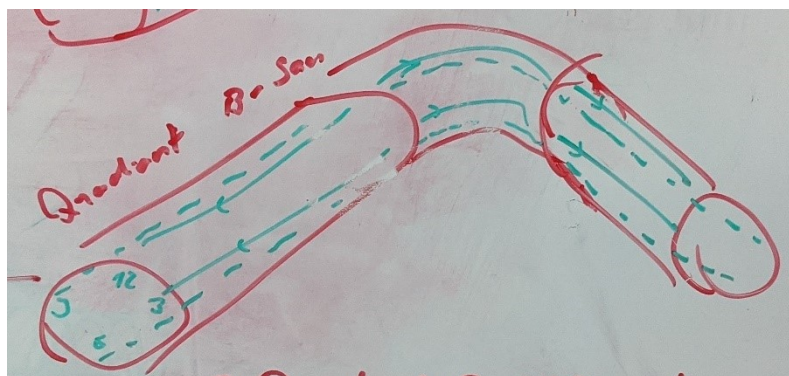


Figure 12: Longitudinal raster.

2.4.2. Calibration

The calibration mockup of Figure 13 was built to allow a reference measurement of a known piece to verify the correct function of the measurement system. A standard UT step gauge with thicknesses ranging from 2.5 to 25 mm is used. It is inlayed into an 8 inch pipe to account for the impact of the surface curvature on the crawler kinematics that may influence the sensor performance.

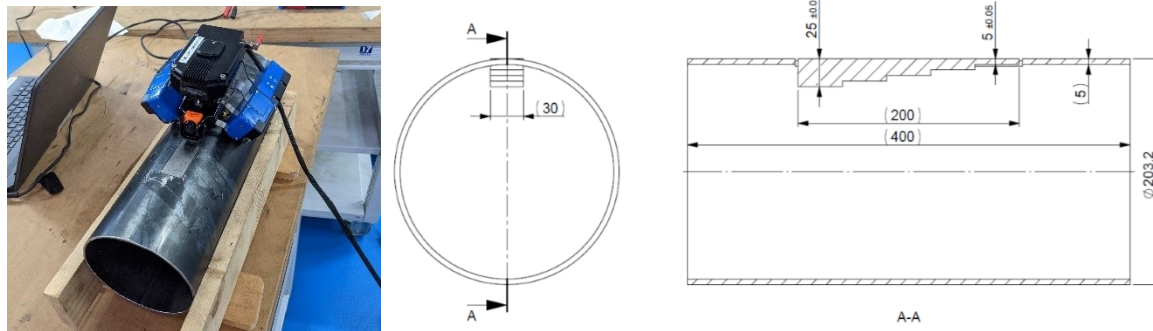


Figure 13: Calibration mockup.

See section Figure 13 for the respective UT measurement recordings.

2.4.3. Navigation

Previous deliverables contain subsystem testing where the capability of the satellite to follow a predefined path has been tested. This was however done with direct line of sight to the location. Together with the drone it is essentially wireless in respect the operator. Accordingly, line of sight cannot be always assumed. To fulfil the inspection capabilities demanded by the end user requirements, both the position relative to a known feature (e.g., welds) and around the circumference of a pipe must be within a required accuracy.

The first tool to position the crawler is the encoder signal from the magnetic wheels that are sent to the UT instrument on the drone by wire and to the pilot through the wireless link of the drone. To locate the crawler, it is positioned so that the weld is flush with the lower edge of the camera view. In this position, the sensor will be at 80 mm in respect to said weld as seen in Figure 14. The rotation of the crawler is regards to the longitudinal axis of the pipe is likewise fixed by centering the targeted feature in the camera view.

Repeat approaches to the same feature have shown variations in accuracy within ± 2 mm.



Figure 14: Crawler positioning relative to weld.

To determine the circumferential position of the crawler, the cameras and an external reference must be used. This may either be the horizon or another known structure in view that has horizontal or vertical features, such as adjacent horizontal or vertical pipes.

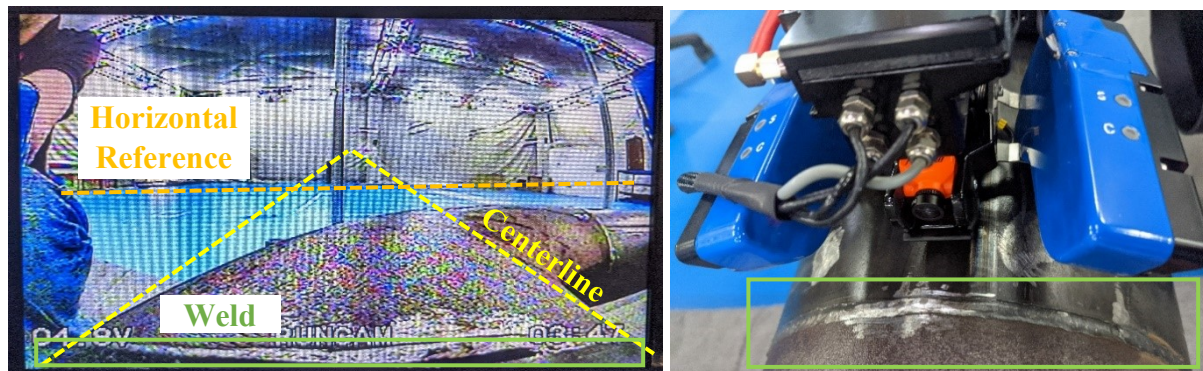


Figure 15: Camera view and references.

While driving, the horizontal or vertical reference must be kept aligned to assure a straight path. Additionally, the pipe being driven on can be kept in the centreline of the image to limit any veering off the pipe axis. Figure 15 is an image of the camera view and the visual references to be used.

2.4.4. Line following horizontal pipe 12 and 6 o'clock

Applying the previously discussed principles to steer the satellite without line of sight, is it possible to drive a straight line at the 12 or 6 o'clock position of a horizontal pipe within an accuracy of ± 20 mm over 2-meter distance. This still satisfies the accuracy requirement of 2 cm from the requirement UR-34. In Figure 16 the actual crawler path is the slightly darker line from the ultrasonic couplant oil.



Figure 16: Horizontal 8'' pipe line scan at 12 o'clock.

2.4.5. Line following horizontal pipe 3 and 9 o'clock

Driving at 3 and 9 o'clock introduces additional error from gravity biasing the crawler path downward. These tests have however shown this effect is limited or easily compensated within the same error margin as other locations. Either due to the relatively low weight of the satellite, little amount of slip from the knurled wheels, or other error factors overshadowing the effect. The slightly darker line in Figure 17 is the crawler path at 3 o'clock.



Figure 17: Horizontal 8'' pipeline scan at 3 o'clock.

2.4.6. Line following horizontal elbow 3 and 9 o'clock

The process for inspecting the 3 and 9 o'clock of the elbow is identical to that on a straight pipe. The same accuracy of under ± 20 mm can be achieved here as well. The darker line in Figure 18 is the ultrasonic couplant oil left by the crawler.



Figure 18: Crawler path along the outside of an elbow.

2.4.1. Line following horizontal elbow 12 and 6 o'clock

For navigation, the sides of the elbow are the most challenging. The pilot must apply constant steering to curve the inspection path along the elbow, while also compensating for any error judged from the camera image. A path as shown in Figure 19 with an error margin of ± 30 mm was shown to be reliably possible for the tested setup.



Figure 19: Path along the top of the elbow.

This exceeds the demanded accuracy of 20 mm in UR-34 and constitutes a limit for the demanded elbow grid inspection in UR-47. A coarser grid consisting of multiple point measurements every ~5 cm instead of a continuous line scan needs to be used for these locations to better achieve a desired positioning for each point.

The alternate satellite design using a hardwire ethernet connection to the drone discussed and tested in previous deliverables could also offer the functionalities needed to achieve the desired accuracy of the line scan. An accelerometer and inclinometer sensors would be available and more advanced position control modes enabled to better steer and track the position of the crawler.

2.4.2. Weld crossing

Welds of up to 3 mm height on the lab testing mockups were successfully passed in any orientation. UR-28 states a should requirement for 5 mm high welds. However, the primary factor whether the crawler can pass is the weld toe angle, as it essentially acts as a ramp for the wheels to climb on. In that regard the welds on the mockup will be a worst case, as they were not manufactured to any kind of quality standard. It is expected that on actual process piping the welds are manufactured to a quality that prescribes a shallower weld toe angle.



Figure 20: Weld crossing tested.

Repeated crossing over the weld in Figure 20 at various speeds and angles did not produce a situation where the crawler loses contact with either of the magnetic wheels.

2.4.3. Surface coating

The impact of a common paint coating was simulated by attaching a non-magnetic to the pipe in Figure 21.



Figure 21: Surface coating test.

UR-25 is the requirement for such a paint layer of 0.3 to 0.5 mm commonly applied as a basic corrosion protection. Should and could requirements of UR-26 and UR-27 for 2 and 3 mm layer thickness respectively would not be achievable with the tested setup. The flying suspension design of the wheels would however allow easy switch to a set of stronger magnets on demand.

2.5. UT results

This section shows the performance of the UT system mounted on the satellite robot of the HMR. First, Section 2.5.1 shows the measurements taken during the calibration phase. In this case, we have used a calibration block with 10 steps to finely tune the sensor parameters (see Figure 22-Figure 31). Once, the sensor is calibrated we show the results collected during the inspection of two different pipes, a straight pipe line and the inspection of a pipe elbow in Section 2.5.2 (see Figure 32) and Section 2.5.3 (see Figure 33), respectively.

2.5.1. Calibration block

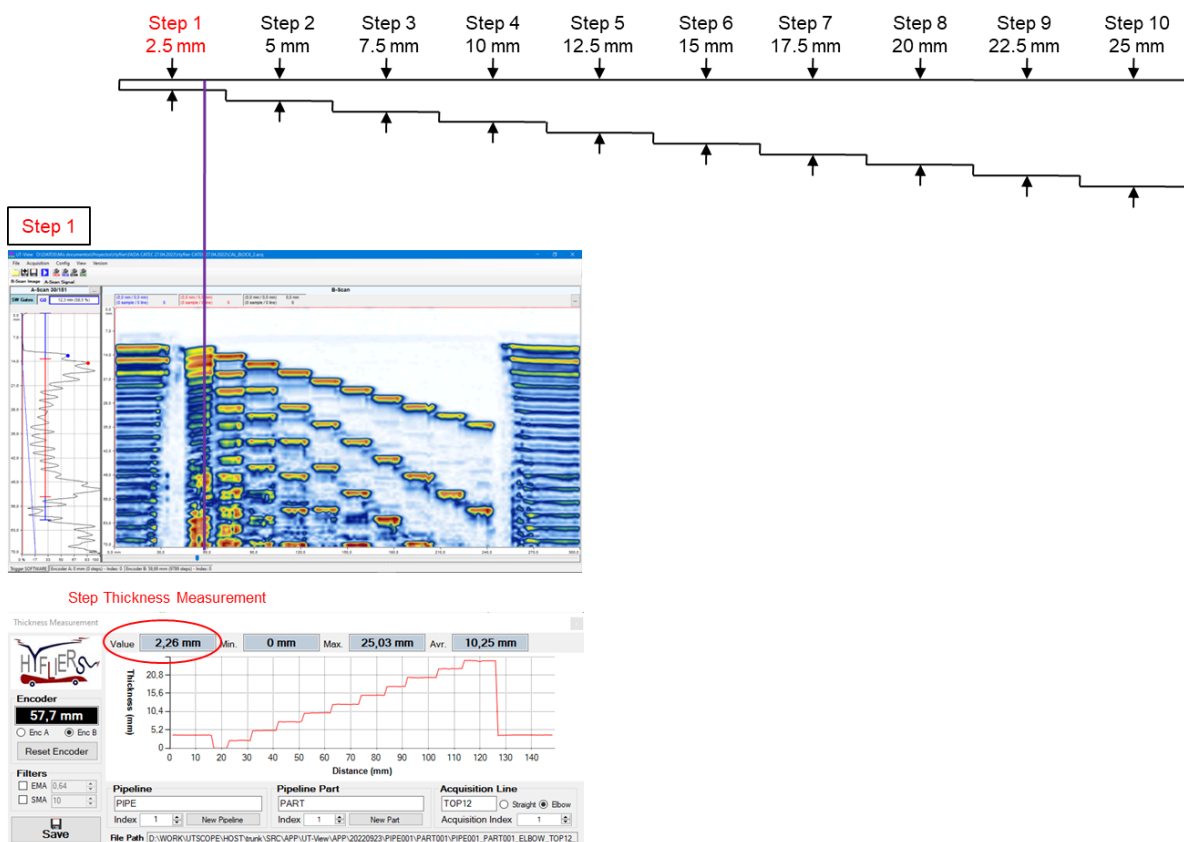


Figure 22: UT calibration S1.

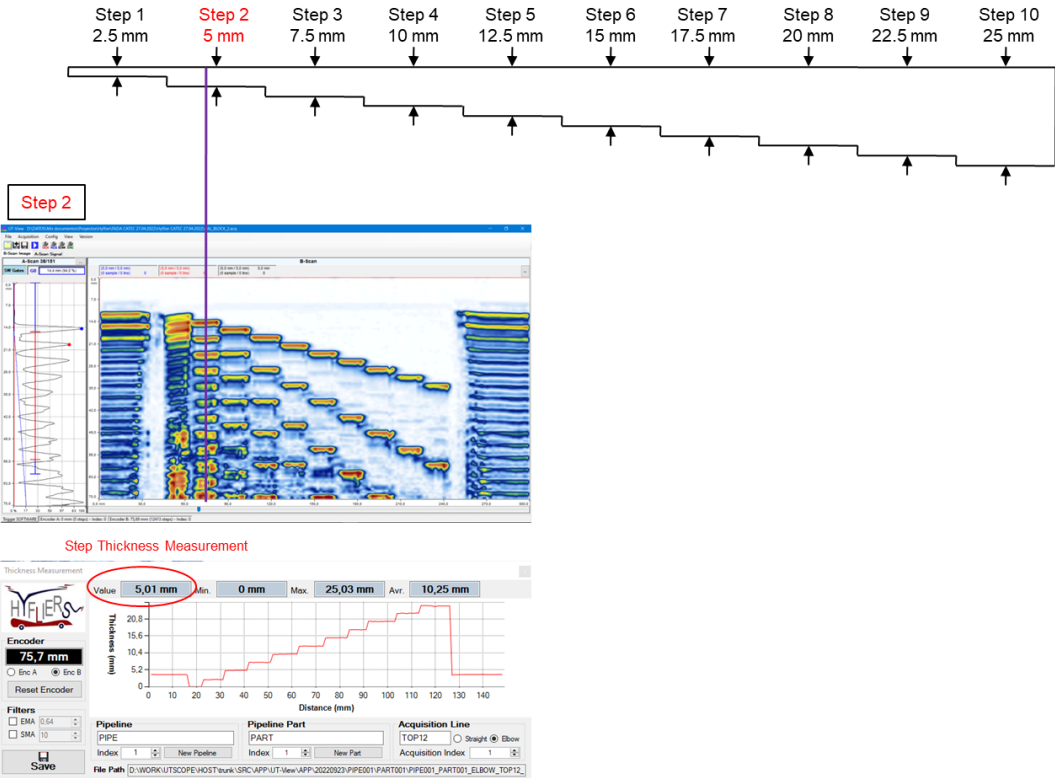


Figure 23: UT calibration S2.

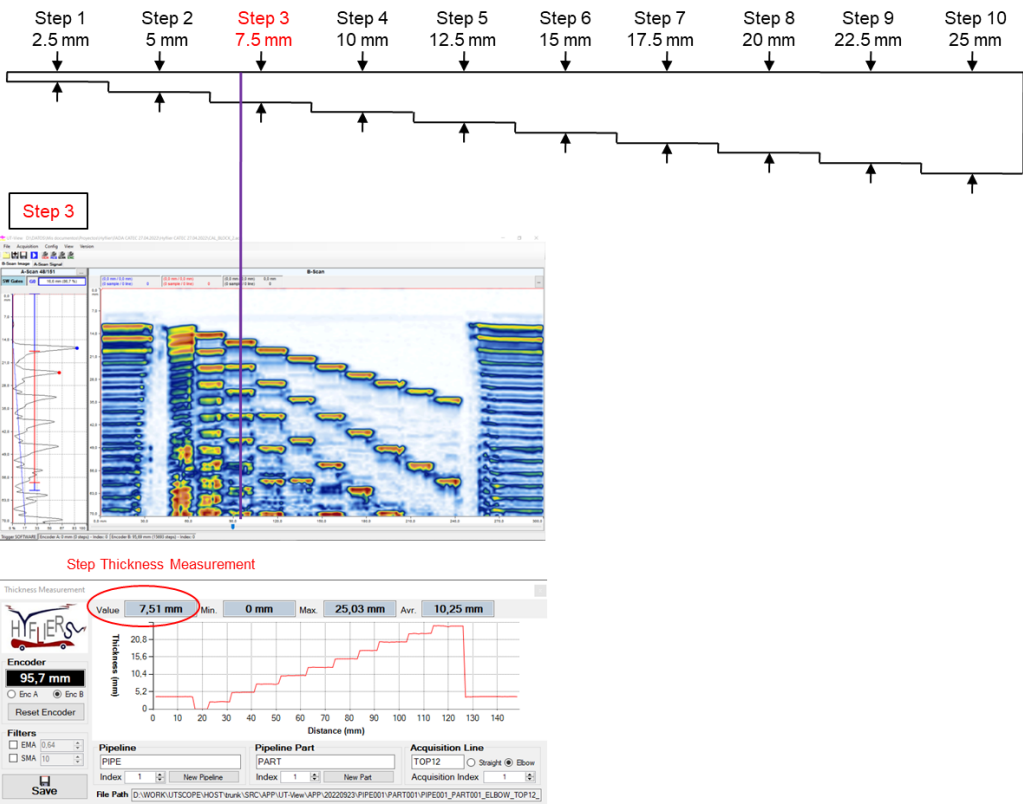


Figure 24: UT calibration S3.

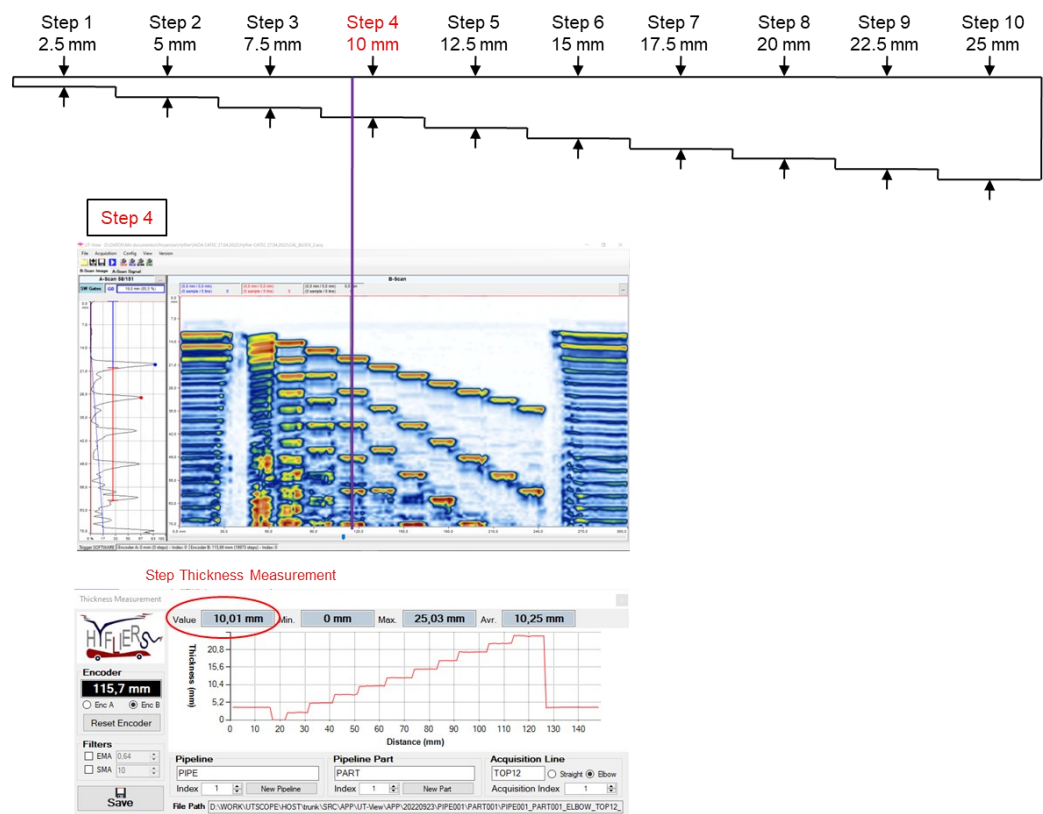


Figure 25: UT calibration S4.

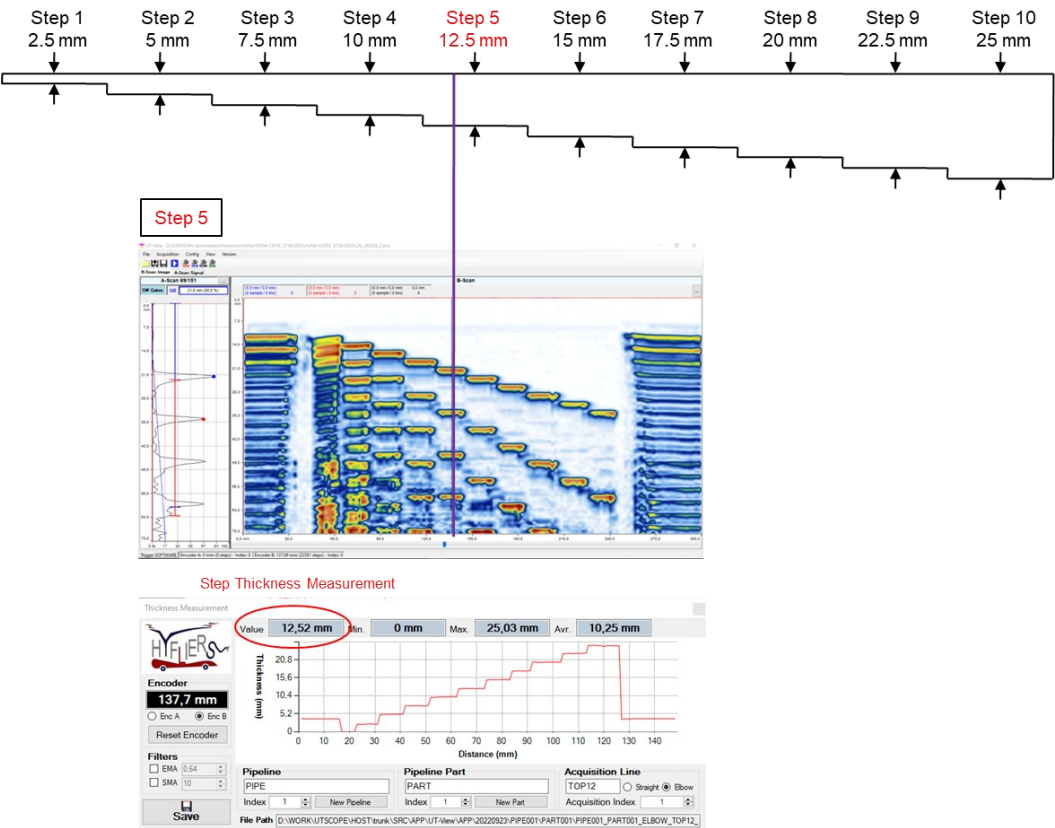


Figure 26: UT calibration S5.

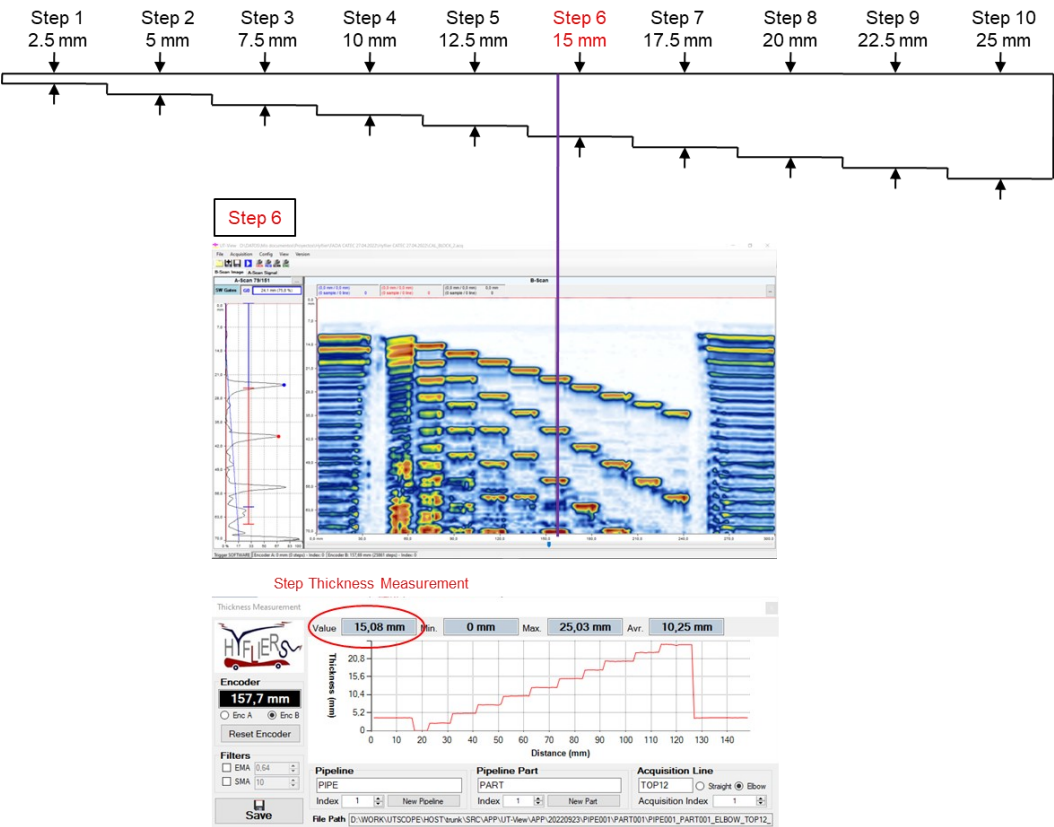


Figure 27: UT calibration S6.

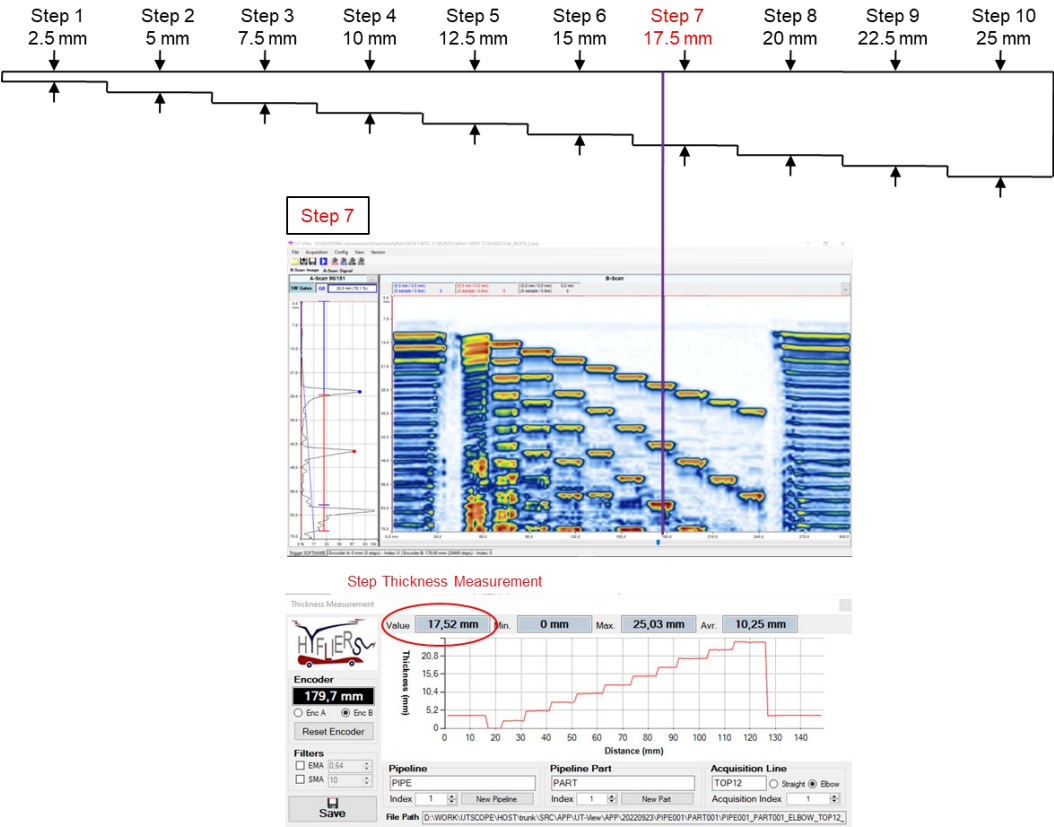


Figure 28: UT calibration S7.

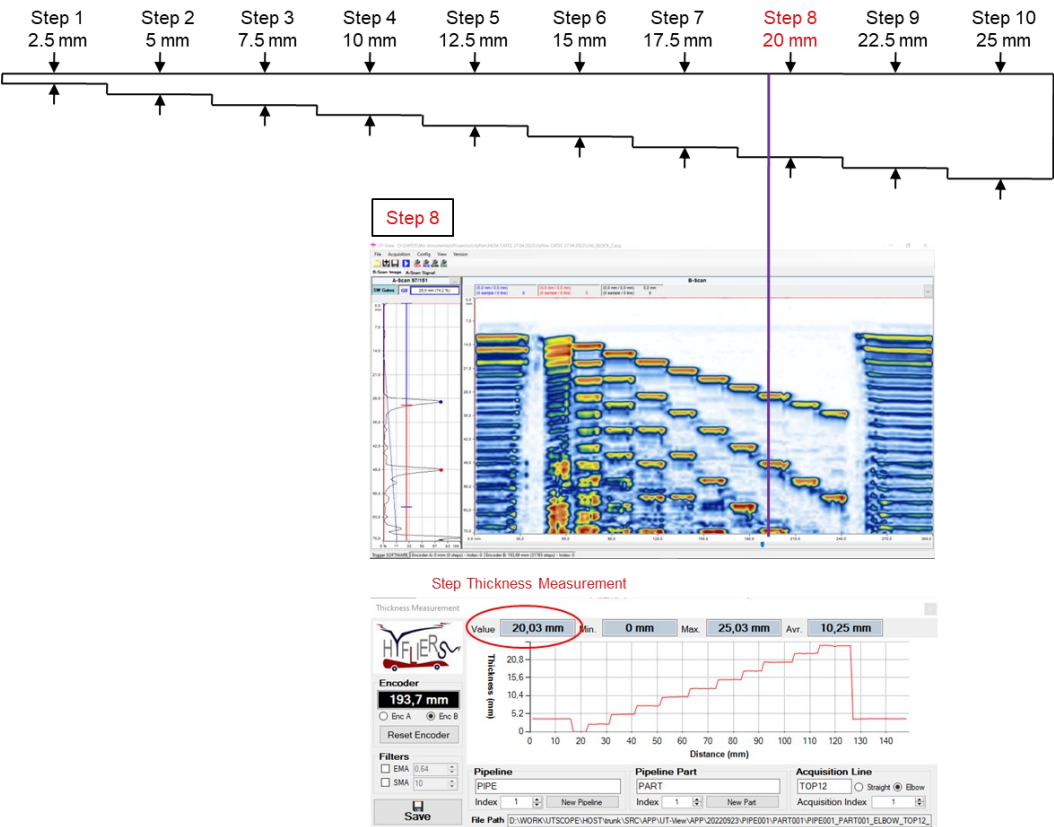


Figure 29: UT calibration S8.

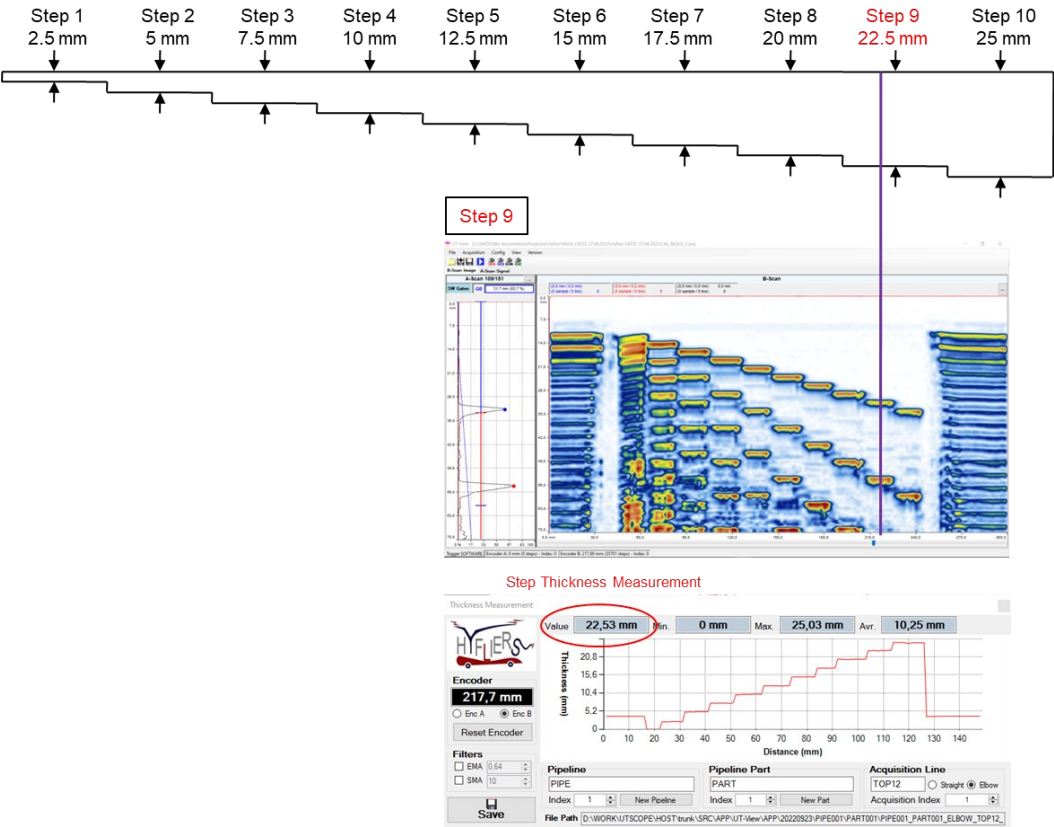


Figure 30: UT calibration S9.

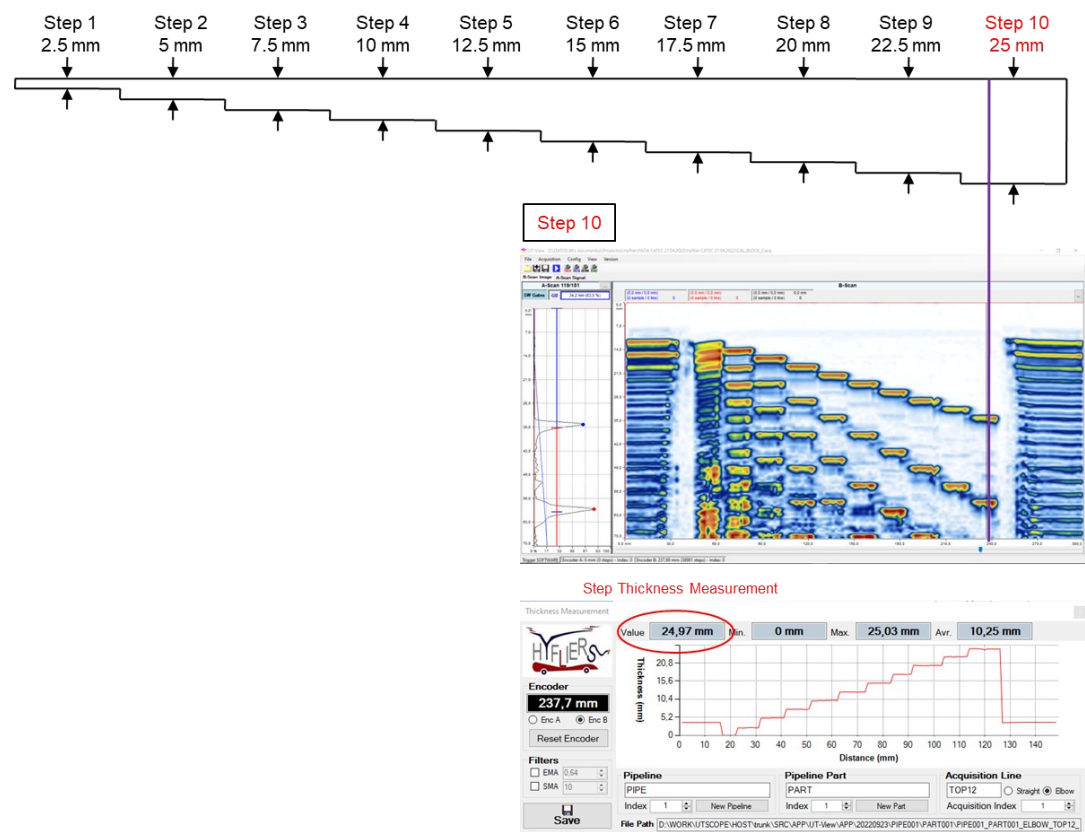
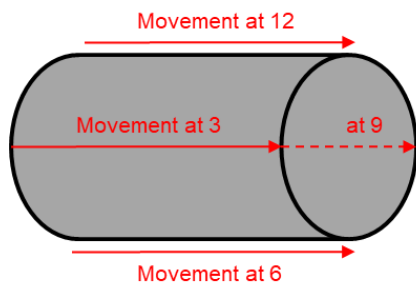
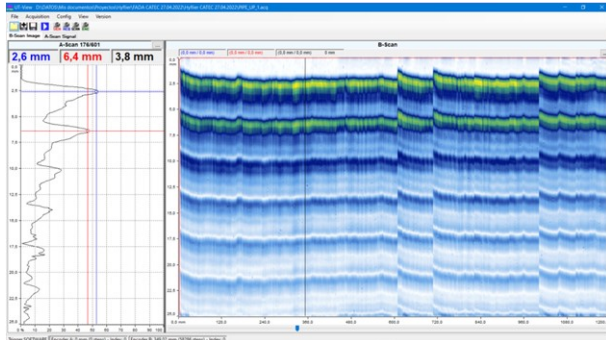


Figure 31: UT calibration S10.

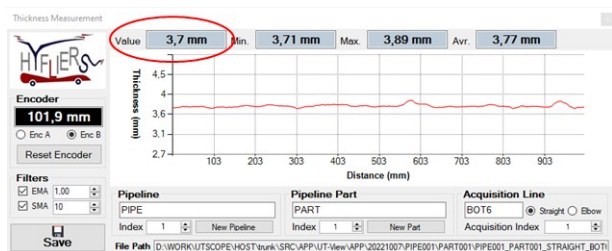
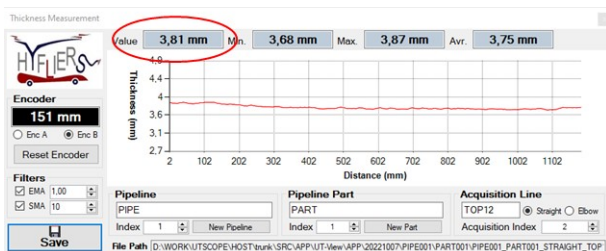
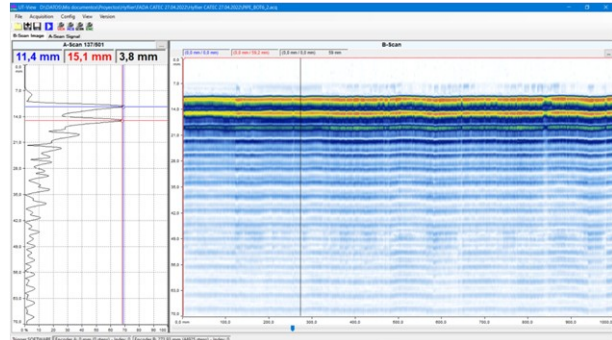
2.5.2. Straight pipe



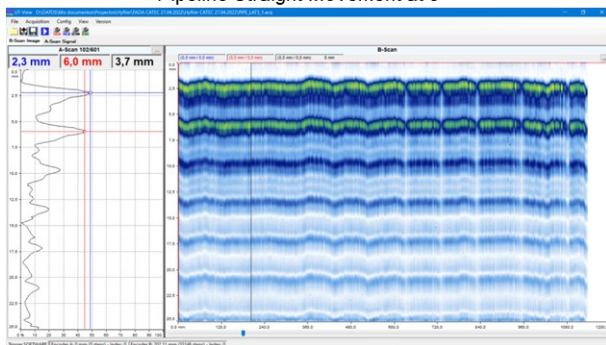
Pipeline Straight Movement at 12



Pipeline Straight Movement at 6



Pipeline Straight Movement at 3



Pipeline Straight Movement at 9

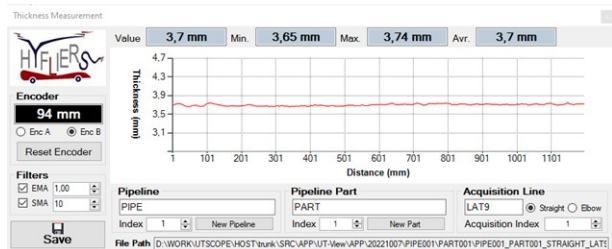
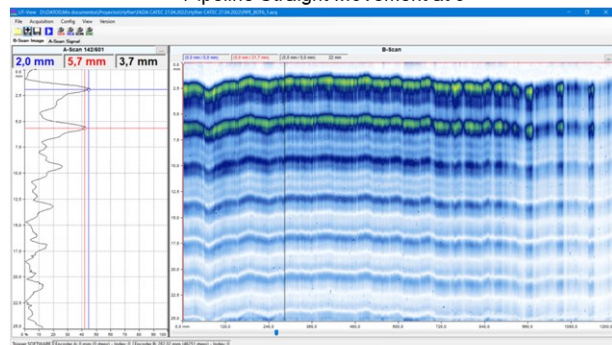
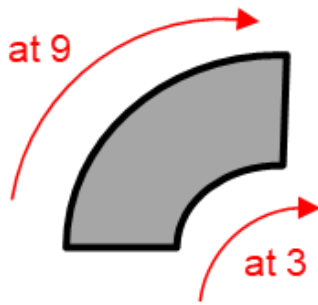
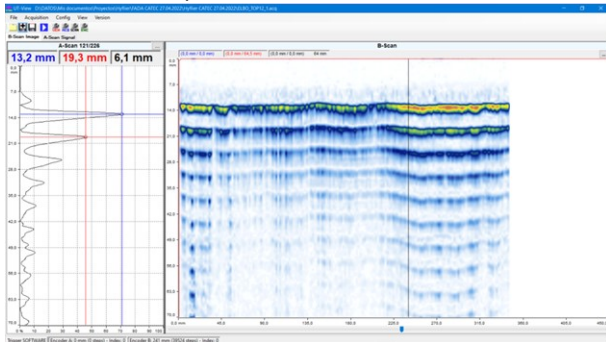


Figure 32: UT straight pipe inspection results.

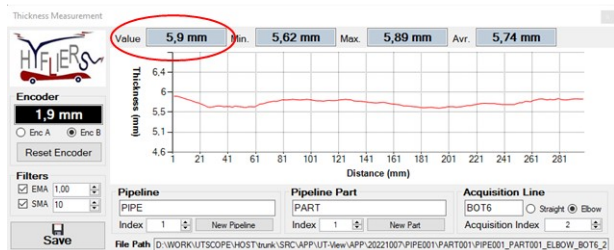
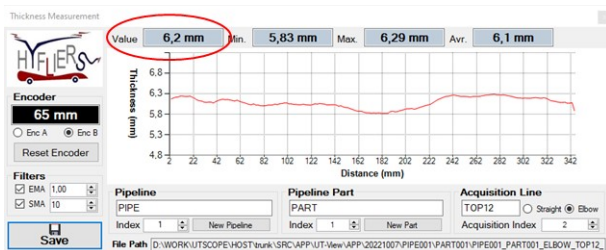
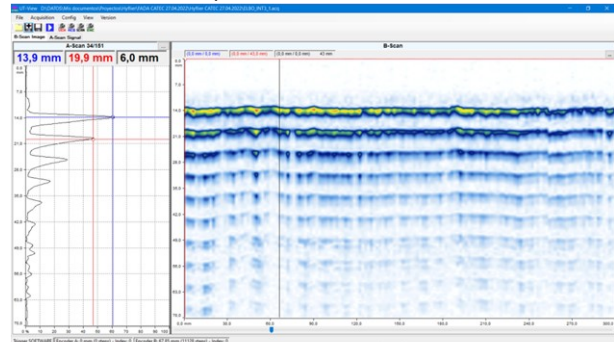
2.5.3. Elbow



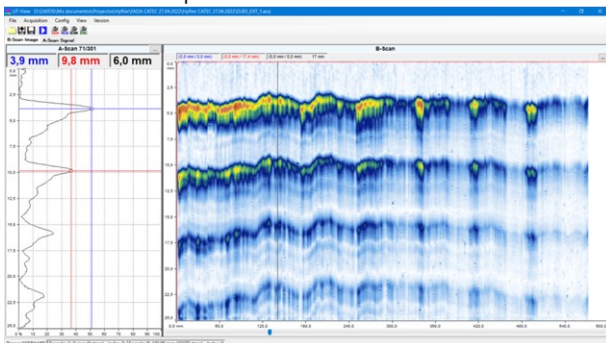
Pipeline Elbow Movement at 12



Pipeline Elbow Movement at 6



Pipeline Elbow Movement at 3



Pipeline Elbow Movement at 9

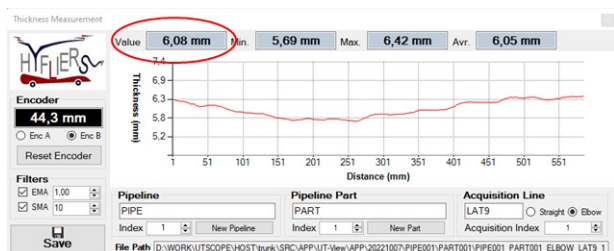
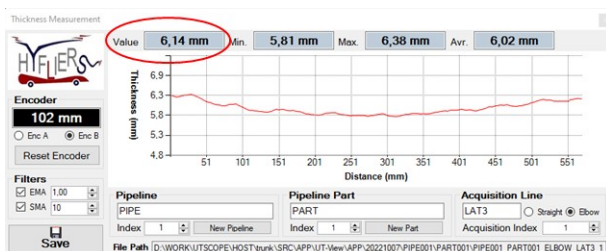
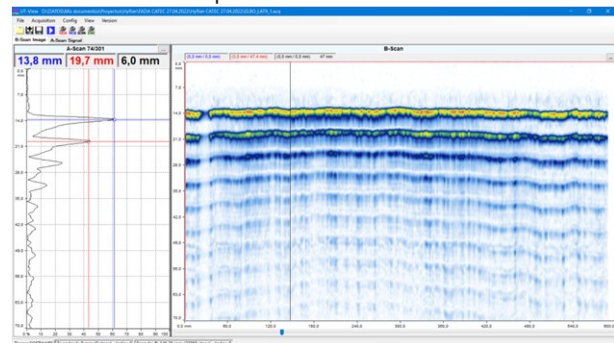


Figure 33: UT elbow inspection results.

2.6. Inspection data processing

As described in D4.3 (Section 4, in particular Figure 1 and the text about it), inspection data are passed from the UT subsystem to the GSDB subsystem of the ground station (see D4.3, Section 4.3).

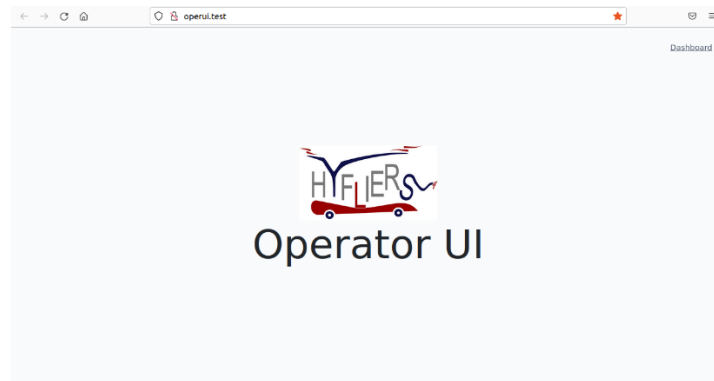



Figure 34: The GSDB UI.

2.6.1. Inspection plan

On the inspection engineer UI, Figure 34, it is first created an inspection plan, see Figure 35. When ready for the inspection to take place, the GSDB subsystem is activated for data reception, see Figure 36.

 Operator UI

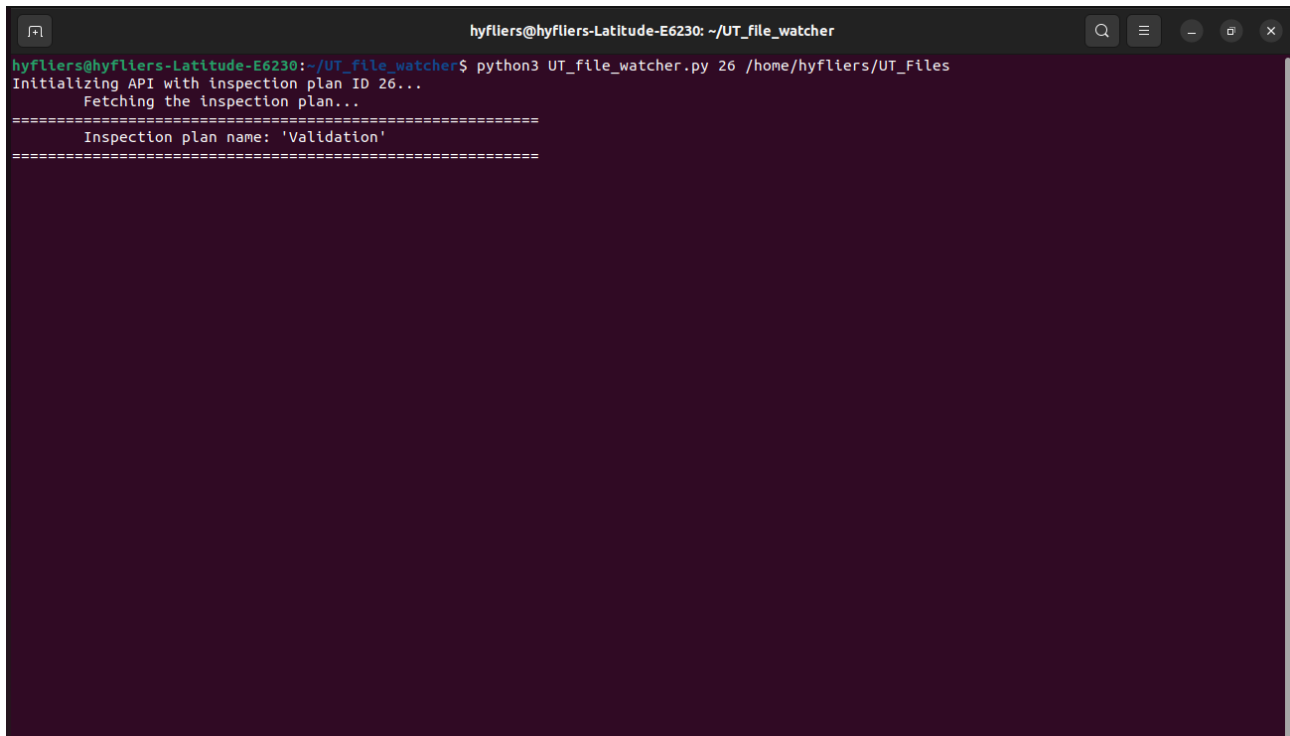
[Clients](#) / [HYFLIERS](#) / Validation

Inspection plan		Edit
ID: 26		
Validation		
Has no inspection report		
Inspection site: CATEC Test Site Inspection site address: C. Wilbur y Orville Wright 19, 41300 Seville, Spain		

[Generate report](#)
[Export PDF](#)

Inspection locations			
ID	Functional location	Scan point location	Scan(s)
166	PIPE001_PART001_STRAIGHT	selected point	None
167	PIPE001_PART001_ELBOW	selected point	None
Total: 2			

Figure 35: Inspection plan for the preliminary validation tests.

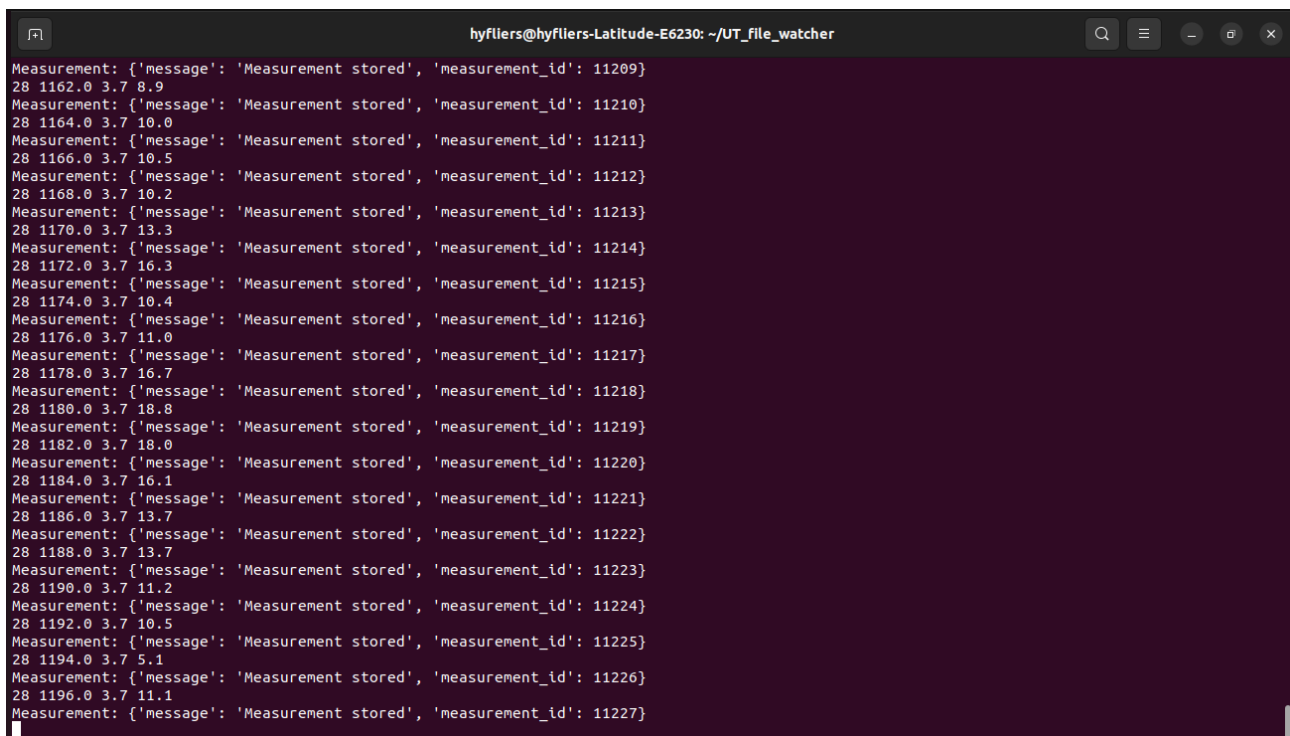


```
hyfliers@hyfliers-Latitude-E6230: ~/UT_file_watcher
hyfliers@hyfliers-Latitude-E6230:~/UT_file_watcher$ python3 UT_file_watcher.py 26 /home/hyfliers/UT_Files
Initializing API with inspection plan ID 26...
Fetching the inspection plan...
=====
Inspection plan name: 'Validation'
=====
```

Figure 36: GSDB subsystem waiting data from the UT subsystem.

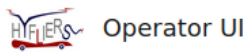
2.6.1. Straight pipe

After the inspection has started, the GSDB subsystem starts receiving inspection data, see Figure 37, with the inspection report being populated. Figure 38 shows the scans for the four quadrants of the straight pipe stored into the database.



```
hyfliers@hyfliers-Latitude-E6230: ~/UT_file_watcher
Measurement: {'message': 'Measurement stored', 'measurement_id': 11209}
28 1162.0 3.7 8.9
Measurement: {'message': 'Measurement stored', 'measurement_id': 11210}
28 1164.0 3.7 10.0
Measurement: {'message': 'Measurement stored', 'measurement_id': 11211}
28 1166.0 3.7 10.5
Measurement: {'message': 'Measurement stored', 'measurement_id': 11212}
28 1168.0 3.7 10.2
Measurement: {'message': 'Measurement stored', 'measurement_id': 11213}
28 1170.0 3.7 13.3
Measurement: {'message': 'Measurement stored', 'measurement_id': 11214}
28 1172.0 3.7 16.3
Measurement: {'message': 'Measurement stored', 'measurement_id': 11215}
28 1174.0 3.7 10.4
Measurement: {'message': 'Measurement stored', 'measurement_id': 11216}
28 1176.0 3.7 11.0
Measurement: {'message': 'Measurement stored', 'measurement_id': 11217}
28 1178.0 3.7 16.7
Measurement: {'message': 'Measurement stored', 'measurement_id': 11218}
28 1180.0 3.7 18.8
Measurement: {'message': 'Measurement stored', 'measurement_id': 11219}
28 1182.0 3.7 18.0
Measurement: {'message': 'Measurement stored', 'measurement_id': 11220}
28 1184.0 3.7 16.1
Measurement: {'message': 'Measurement stored', 'measurement_id': 11221}
28 1186.0 3.7 13.7
Measurement: {'message': 'Measurement stored', 'measurement_id': 11222}
28 1188.0 3.7 13.7
Measurement: {'message': 'Measurement stored', 'measurement_id': 11223}
28 1190.0 3.7 11.2
Measurement: {'message': 'Measurement stored', 'measurement_id': 11224}
28 1192.0 3.7 10.5
Measurement: {'message': 'Measurement stored', 'measurement_id': 11225}
28 1194.0 3.7 5.1
Measurement: {'message': 'Measurement stored', 'measurement_id': 11226}
28 1196.0 3.7 11.1
Measurement: {'message': 'Measurement stored', 'measurement_id': 11227}
```

Figure 37: GSDB subsystem receiving data from the UT subsystem.



[Clients](#) / [HYFLIERS](#) / Validation

Inspection plan	Edit
ID: 26	
Validation	
Has no inspection report	
Inspection site: CATEC Test Site	
Inspection site address: C. Wilbur y Orville Wright 19, 41300 Seville, Spain	

[Generate report](#)
[Export PDF](#)

ID	Functional location	Scan point location	Scan(s)
166	PIPE001_PART001_STRAIGHT	selected point	#25 #26 #27 #28
167	PIPE001_PART001_ELBOW	selected point	None

Total: 2

Figure 38: Straight pipe inspection results are collected at the inspection report.

Results of the scans can be seen by clicking on the blue scan icons. Figure 39 and Figure 40 show the visualisation of inspection data of the straight pipe, at its 12 and 6, and 3 and 9 o'clock positions, respectively.

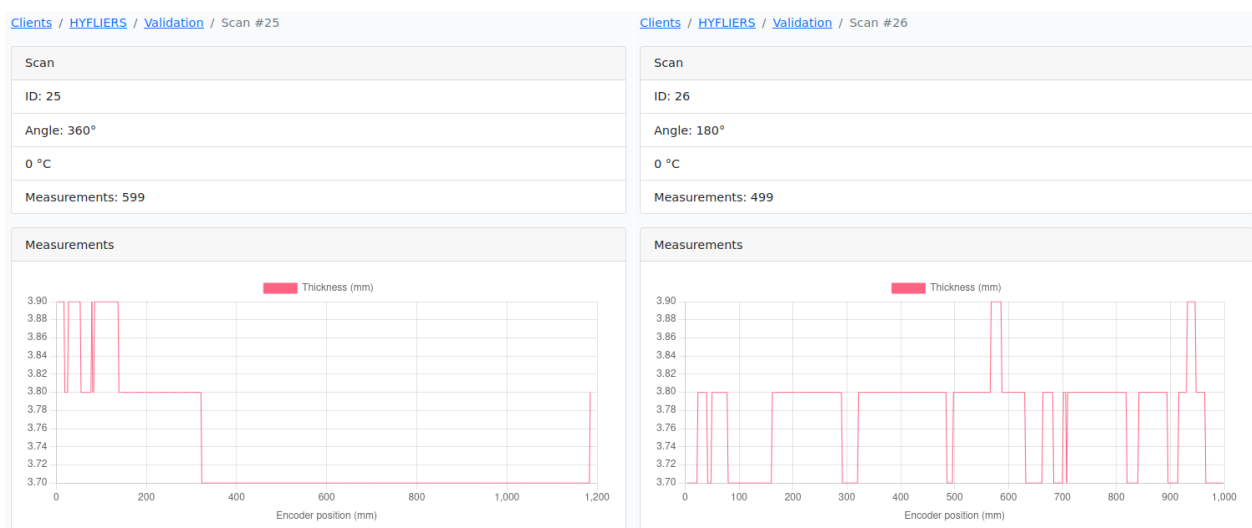


Figure 39: Straight pipe inspection results: 12 o'clock (360°) and 6 o'clock (180°) positions.

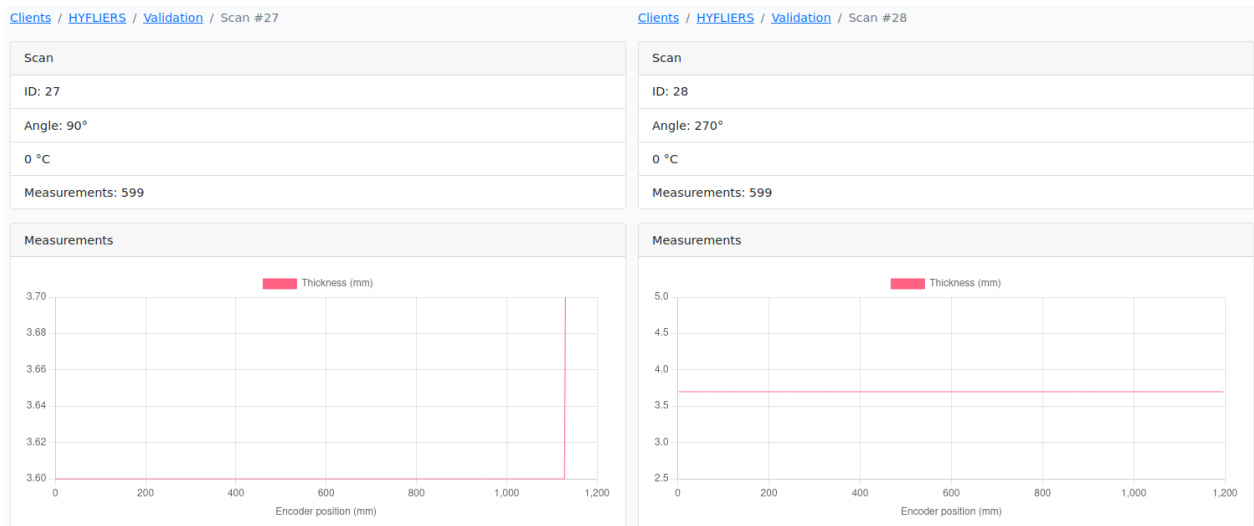


Figure 40: Straight pipe inspection results: 3 o'clock (90°) and 9 o'clock (270°) positions.

2.6.2. Elbow

The next step in the inspection plan is to proceed to the elbow. Figure 41 shows the status when all the four quadrants of the elbow have been inspected and their scans acquired at the database.



Operator UI

[Clients](#) / [HYFLIERS](#) / [Validation](#)

Inspection plan [Edit](#)

ID: 26

Validation

Has no inspection report

Inspection site: [CATEC Test Site](#)
Inspection site address: C. Wilbur y Orville Wright 19, 41300 Seville, Spain

[Generate report](#)
[Export PDF](#)

ID	Functional location	Scan point location	Scan(s)
166	PIPE001_PART001_STRAIGHT	selected point	#25 #26 #27 #28
167	PIPE001_PART001_ELBOW	selected point	#29 #30 #31 #32

Total: 2

Figure 41: Also elbow inspection results are now collected at the inspection report.

Figure 42 shows the visualisation of inspection data of the elbow at its top and bottom positions. Figure 43 displays inspection data visualisation of the same pipe at its the data collected at its internal 3 o'clock and external 9 o'clock positions.

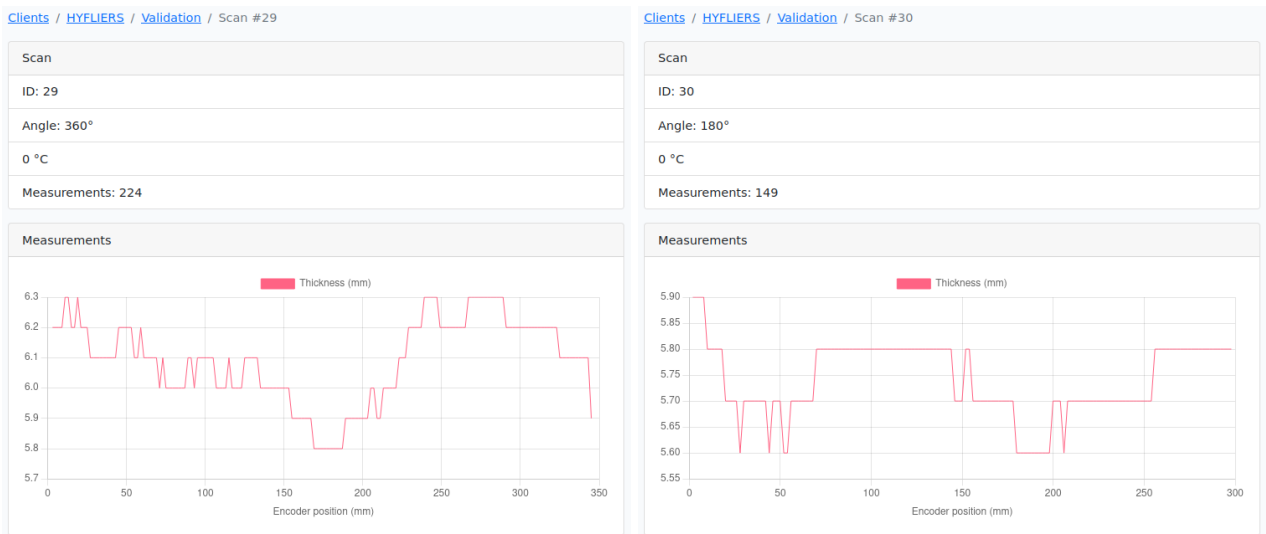


Figure 42: Elbow inspection results: 12 o’clock (360°) and 6 o’clock (180°) positions.

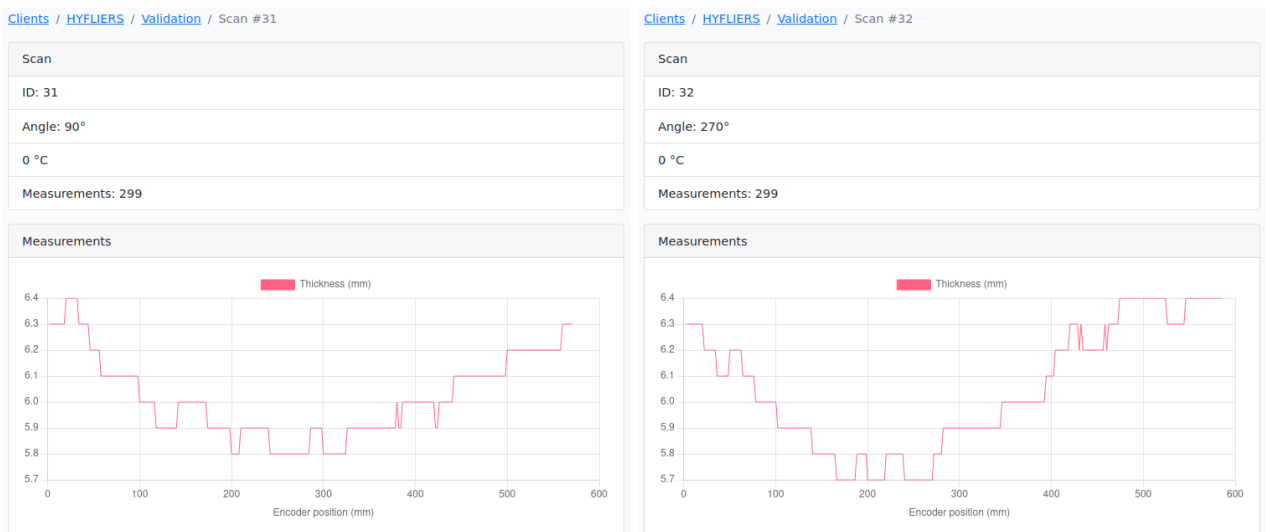


Figure 43: Elbow inspection results: 3 o’clock (90°) and 9 o’clock (270°) positions.

2.6.3. Inspection report

When all the inspection locations have been inspected, the inspection report can be generated (see the blue button in Figure 41), so that it can be found in the database, see Figure 44.

[Clients](#) / [HYFLIERS](#) / Report #2600

Inspection report	Edit
ID: 11	
Report n:o: 2600	
Contract n:o: 2601	
Inspection plan: #26	
Inspection site: CATEC Test Site	
Inspection site address: C. Wilbur y Orville Wright 19, 41300 Seville, Spain	

[Export PDF](#)

Inspection locations			
ID	Functional location	Scan point location	Scan(s)
166	PIPE001_PART001_STRAIGHT	selected point	#25 #26 #27 #28
167	PIPE001_PART001_ELBOW	selected point	#29 #30 #31 #32
Total: 2			

Figure 44: The inspection report for the preliminary validation tests as visualised on the support tool.

2.7. Full experiments

This section shows a sequence of images (from Figure 45 to Figure 49) of a full inspection operation accomplished in the outdoors mock-up scenario prepared in the context of the HYFLIERS project.



Figure 45: HMR takes off and looks for the pipe.



Figure 46: HMR during orientation and landing phases.



Figure 47: HMR landed on pipe.

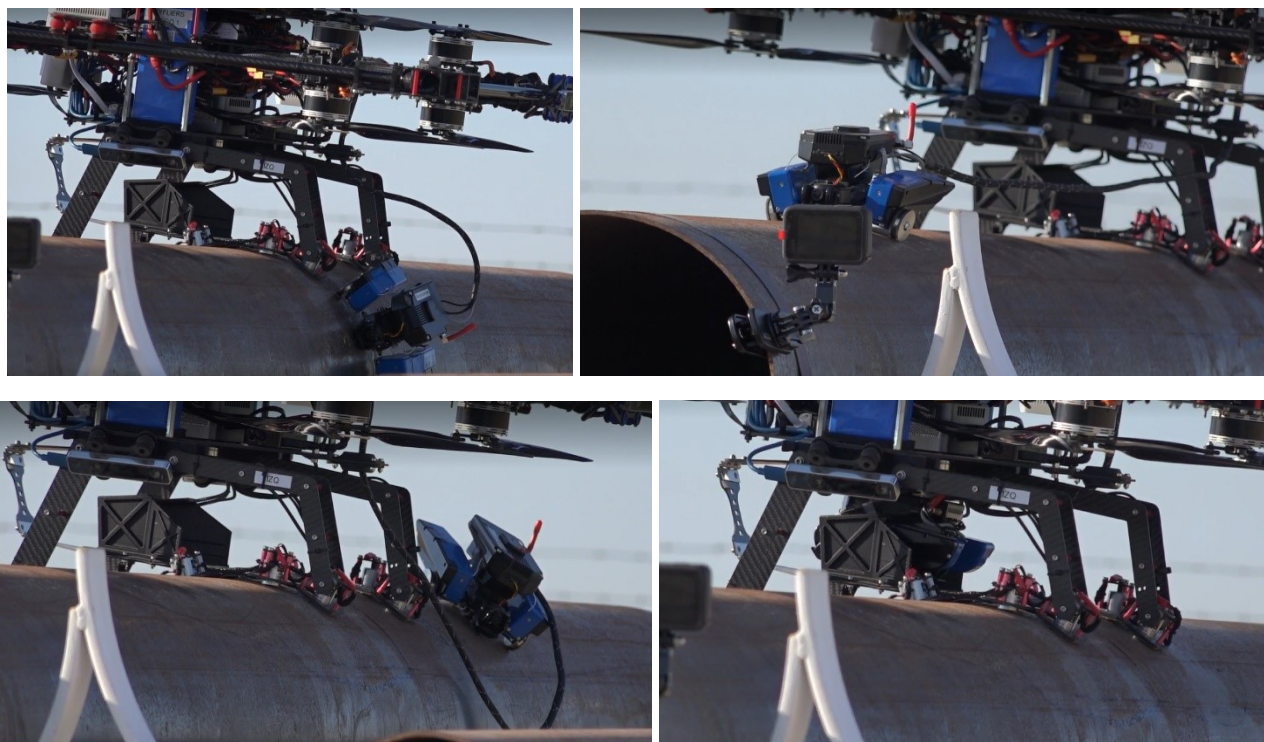


Figure 48: HMR satellite moving over the pipe.

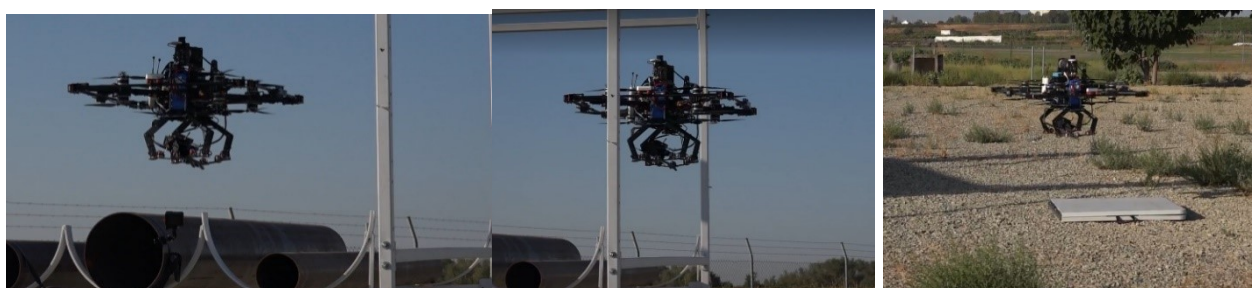


Figure 49: HMR takes off and returns home.

3. HRA experiments

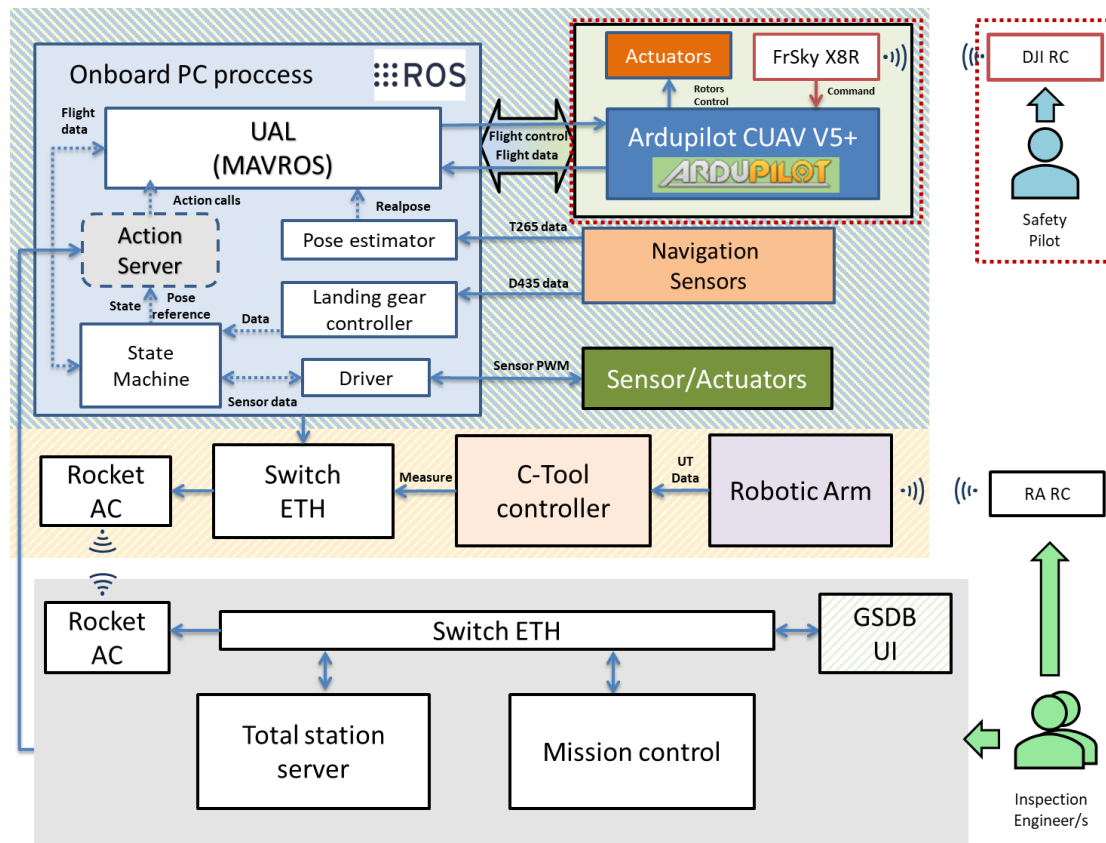


Figure 50 HRA software architecture.

Figure 50 shows the HRA software architecture presented in deliverable D5.2. The HRA uses two main onboard computers to split the low-level flight control from the autonomous functionalities. It has four main software subsystems, which are the aerial HRA control module, the localization and navigation subsystem, the landing gear controller, and the C-Tool manipulator controller.

As it was presented in deliverables D2.1 and D2.2, the HRA modular design provides for different add-ons at the landing gear to cope with various pipe configurations, although, for the final integrated prototype, the crawler clamp has been used with the C-Tool. In the following sections are presented experimental tests of the HRA with the rolling and the crawler clamp landing gears. Integration experiments with the arm and an experiment with the final prototype are also presented.

3.1. Testing of the HRA rolling landing gear add-on.

The tests have been done with the HRA prototype with the rollers landing gear add-on described in D2.2, which is intended for landing and operation on pipe racks with small or no separation between the pipes. These experiments test the validity of the roller design, the aerial controller, the navigation system and the landing gear controller.

The experiments have been performed in the outdoor scenario shown in Figure 51, consisting of two arrays of three PVC pipes (2 m length, 20 cm diameter, 10 cm separation) supported by a frame structure built with Rexroth bars.

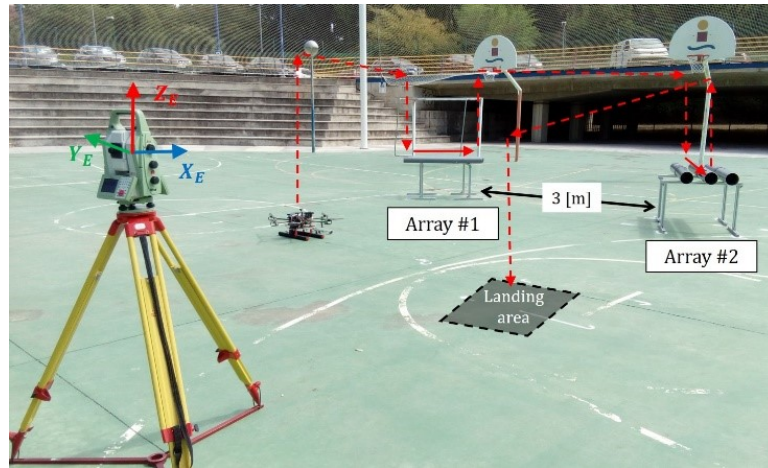


Figure 51 Outdoor validation scenario with two arrays of pipes.

The path of the aerial robot is provided by a path planner, and is divided into thirteen phases: 0) take-off, 1) go to the landing point on the first array, 2) land, 3) roll towards the first inspection point, 4) inspect the pipe, 5) take-off, 6) go to the landing point on the second array, 7) land, 8) roll towards the second inspection point, 9) inspect the pipe, 10) take-off, 11) go back to the initial position, 12) land. Once the robot has landed on the array, the rolling base is tele-operated by the inspector who follows the planned path and visually inspects the pipe with the capability of taking high-level decisions related to the inspection. The execution of the experiment can be followed in the sequence of images depicted in Figure 52.

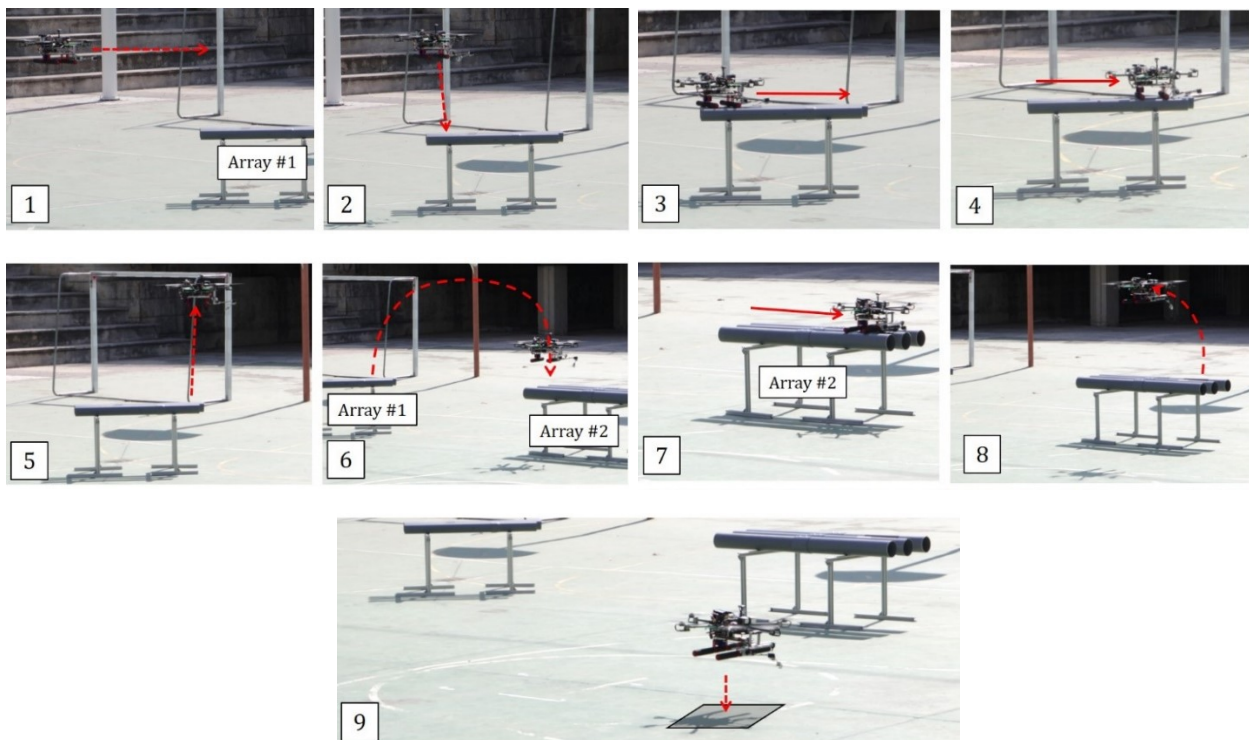


Figure 52 Sequence of images showing the experiment.

Additionally, Figure 53 presents the trajectory executed by the HRA with the rollers add-on along with its reference path. The evolution of the position and orientation of the hybrid rolling-aerial

platform is shown in Figure 54, where the different aerial and on-pipe phases can be observed, as well as the take-offs and landings.

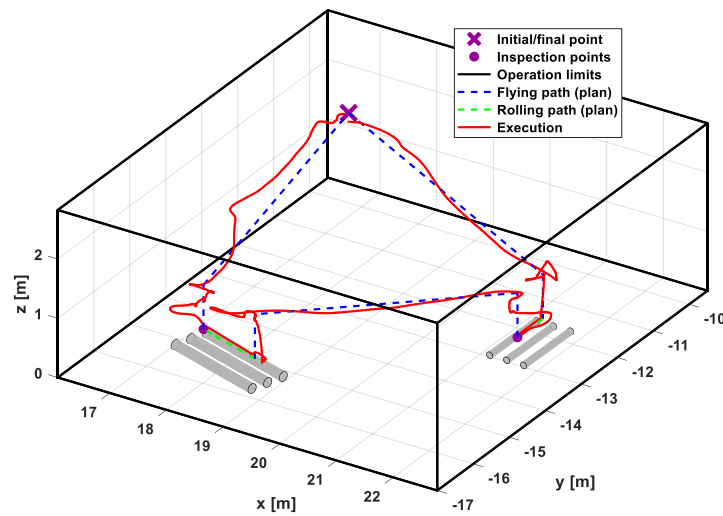


Figure 53 Reference path and execution of the path by the HRA.

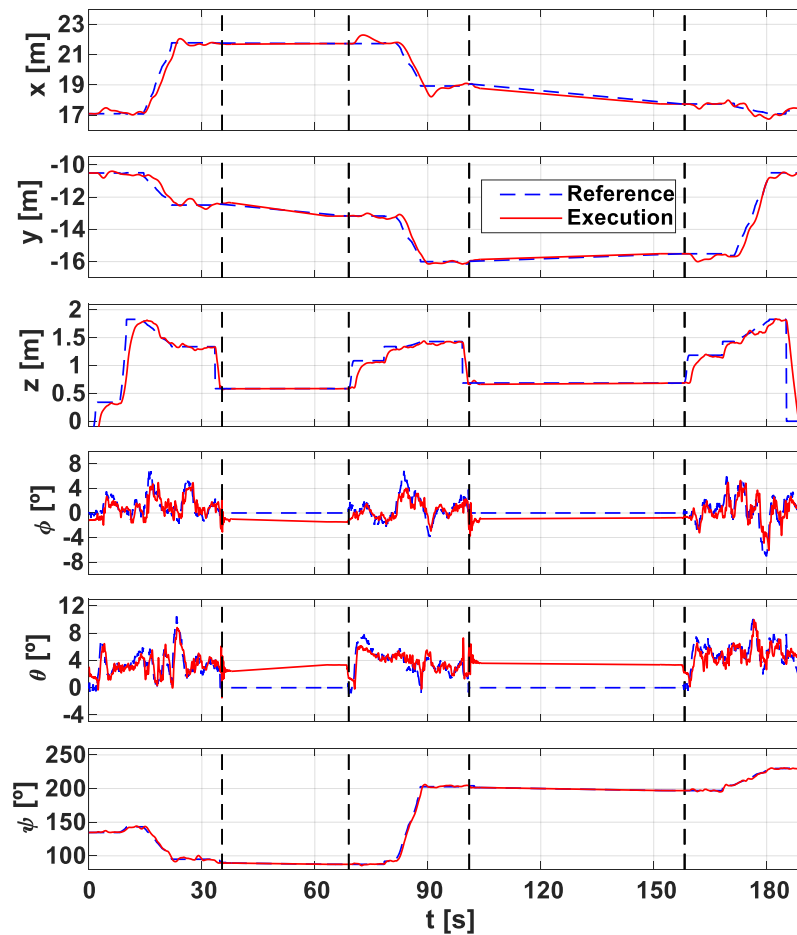


Figure 54 Evolution of the multirotor position and orientation during the experiment.

3.2. Testing of the HRA with the crawler clamp landing gear add-on.

The experiments shown in this section have been done with the final prototype with the C-Tool in the Seville outdoors mock-up scenario, as seen in Figure 55 (a complete experiment is shown in Section Figure 69). The experiment shows the approach to the pipe, landing on the pipe, the movement of the HRA over the pipe using the actuators of the landing gear while actively maintaining stability over the pipe, take-off and move away from the pipe.

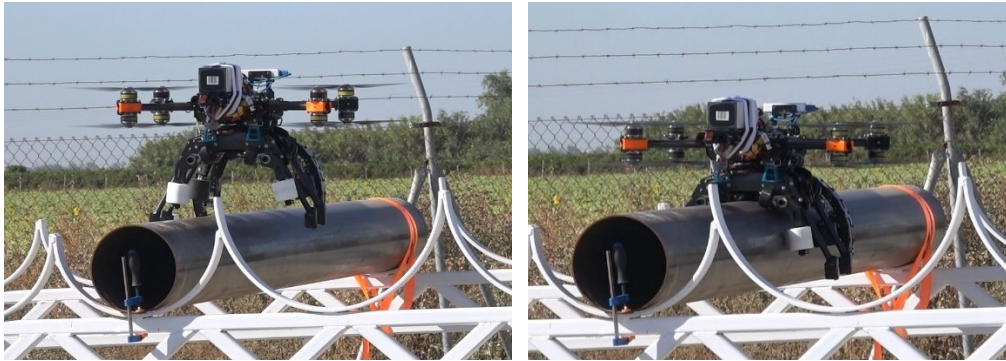


Figure 55 Experiment with HRA with crawler clamp.

Figure 56 shows the pitch and roll attitude angles of the HRA during the experiment. The different phases are separated by vertical dashed lines in the plots of the figure. In the first phase, the HRA is flying in the air and the aerial controller takes care of the control and stabilization of the attitude angles. Once the HRA lands on the pipe, marked by the first dashed line, the pitch angle becomes constrained by the pipe and remains almost constant during the movement of the HRA over the pipe (the small variation of the pitch angle is due to variations in the inclination of the HRA caused by variations in the speed and the friction of the contact of the landing gear with the pipe).

The roll angle on the other hand is free to vary when the HRA is on the pipe, since it corresponds to the rotation of the HRA around the pipe. This angle must be controlled and stabilized, since the goal is to maintain the HRA always on top of the pipe (roll reference of 0 degrees).

Figure 56 shows that just after the landing the roll angle is 2.2° , but then the stabilization controller begins to work and rapidly takes it to decrease, maintaining the roll angle between $\pm 1.5^\circ$ all the time the HRA is on the pipe.

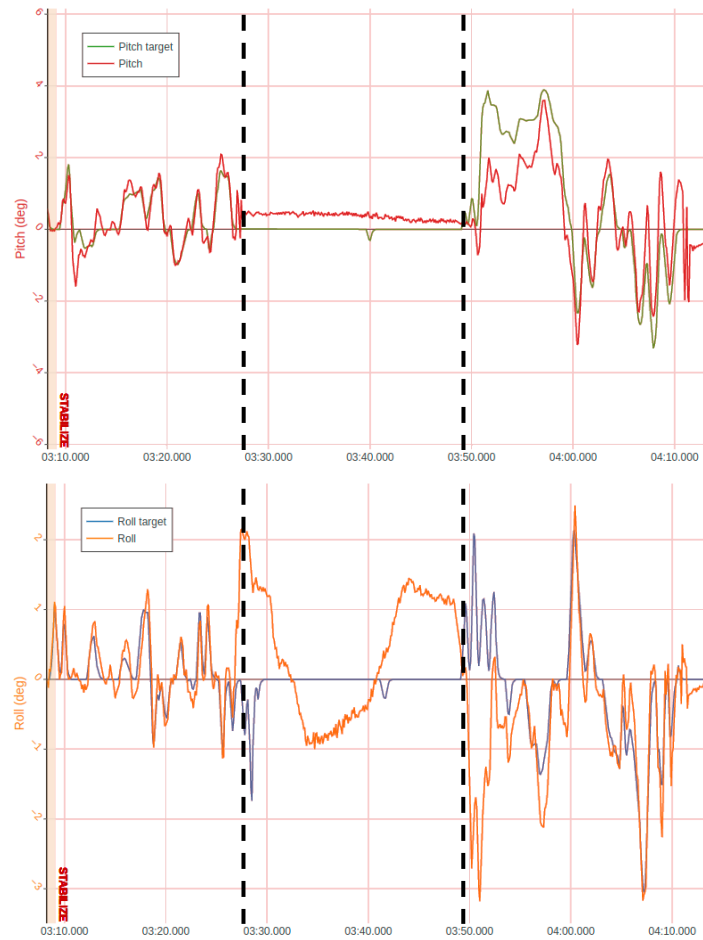


Figure 56 Pitch and roll attitude angles of the HRA with crawler clamp during the experiment.

3.3. Arm

The inspection Arm has been tested with the CREATE hybrid aerial platform, shown in Figure 57.

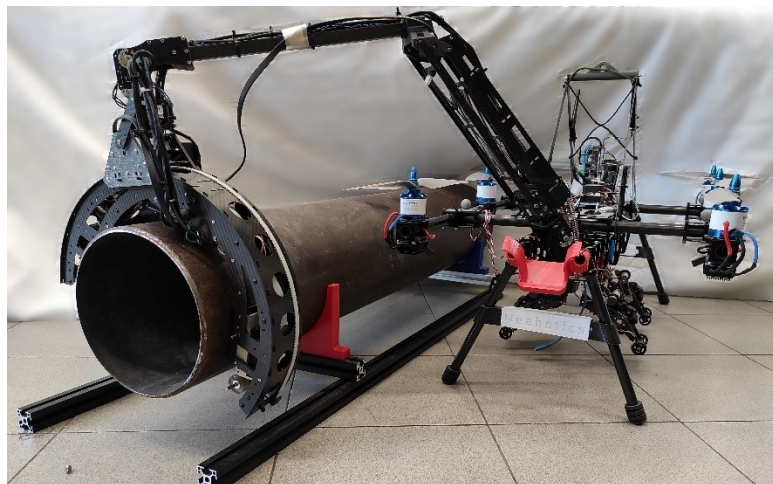


Figure 57: Prototype of the hybrid aerial-ground mobile manipulator for thickness inspection.

The system architecture of the CREATE HRA is depicted in Figure 58.

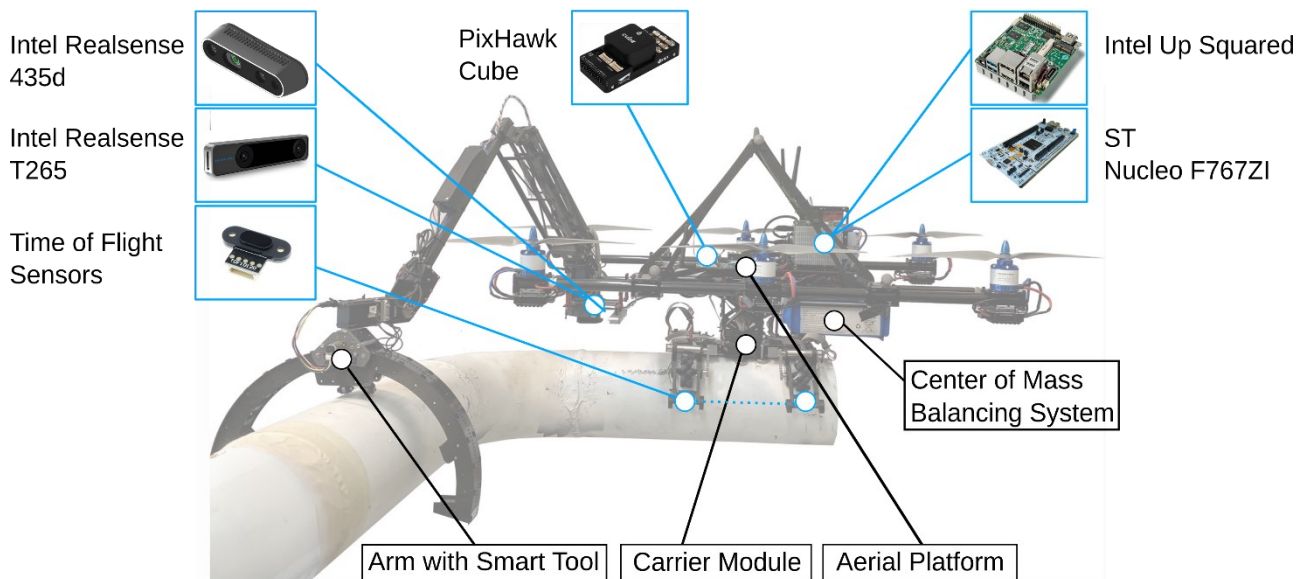


Figure 58: Prototype of the hybrid aerial-ground mobile manipulator for thickness inspection.

The HRA system can be split into three modules: an in-line six-rotor aerial platform, an articulated carrier module, and a robotic manipulator endowed with the C inspection tool (C-Tool).

Three computation units control the whole system. The low-level system is controlled by a classical micro controller board that directly manages the robot's actuators. The aerial unit is controlled via a commercial autopilot (PixHawk Cube). Finally, the high-level capabilities are managed by a companion computer. Such a computer can be used to establish the communication between the platform and the human operator and enable the perception capabilities along with platform localization and stabilization during the flight also in GPS-denied environments. As for the sensors, the robot has been equipped with a depth camera (Intel RealSense 435d) and a motion tracking camera (Intel RealSense t265) to elaborate information about the world and track the position of the platform, respectively.

Two main tests have been performed to demonstrate the effectiveness of the anthropomorphic arm in reaching desired inspection positions transporting the C-Tool inspection capabilities.

The first test case has been performed in the CREATE flight arena (see Figure 59).

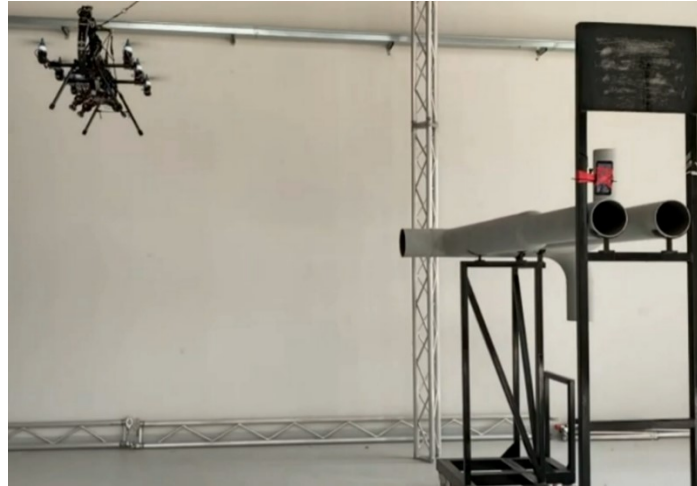


Figure 59: Laboratory mock-up with two adjacent pipes.

Here, the robot must take off from the ground and land on the inspection point. After landed, the manipulator is used to wrap the pipe to inspect. Then, the system is commanded to take off from the pipe and land on the ground to conclude the inspection procedure. The aerial system is equipped with a PixHawk control board as system autopilot, running the open-source control framework PX4. For the take-off, the standard routine provided by the system autopilot is used. After this phase the robot is commanded in proximity of the pipe rack. During this stage, the inspection arm is folded in its resting position, and the system weight is balanced, maintaining its centre of gravity equal to its centre of mass. When the UAV is over the pipe rack, the landing procedure starts. In this context, when the robot reaches the pipe surface, the autopilot automatically detects the landing state and disarms the drone disabling its avionics.

After landed, the arm is unfolded, and the inspection procedure is invoked to wrap the pipe using the smart tool. The tool can rotate 180 degrees (90 degrees in the clockwise direction and 90 degrees in the counter clockwise direction) to inspect the whole surface of the tube. This process is shown in Figure 60. Finally, when the pipe section has been inspected, the arm is folded to take off from the pipe. Also, here, the take-off routine of the autopilot is used, while the stabilization behaviour is disabled when the platform is flying.

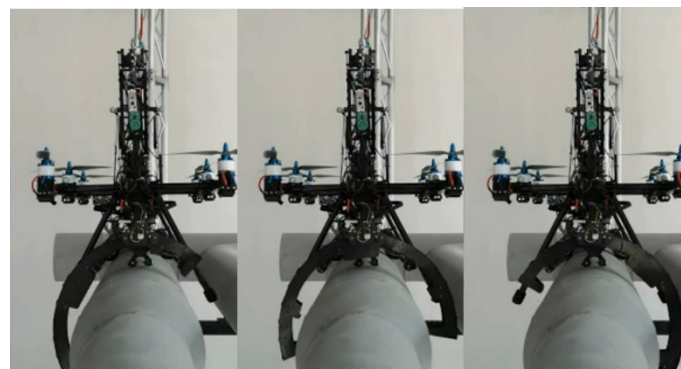


Figure 60: Pipe inspection procedure: rotation in clockwise direction, initial position, rotation in counter-clockwise direction.

During this test, the effectiveness of the stabilization controller and the manipulability of the arm are assessed considering the motion of the manipulator when it is operated over the pipe.

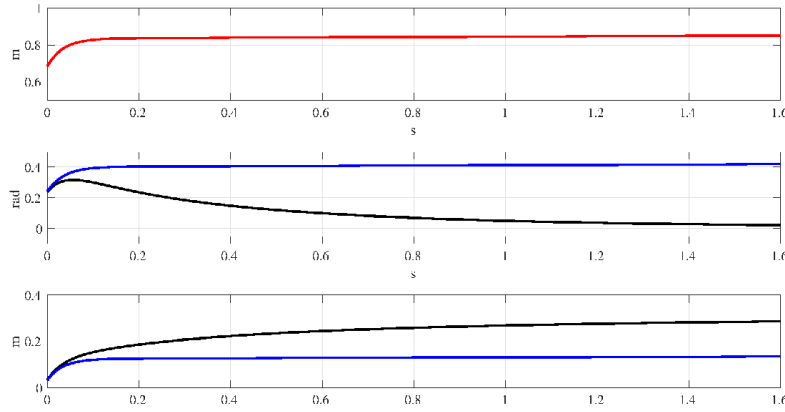


Figure 61: Elbow position during a longitudinal motion of the end-effector. The position of the mobile base over the pipe is commanded to maintain the elbow joint closer to the body of the platform. From top to bottom, the position of the end-effector in the longitudinal direction, the error of the elbow with respect to the desired angle and the position of the rover along the pipe. In blue the same data without the projection onto the null space (the curves in blue are the upper curve in the mid subfigure and the lower curve in the bottom subfigure).

The COM task is used to maintain the Center of Mass of the robot as close as possible to the center of the airframe. For this reason, high number of degrees of freedom of the platform is used, as shown in Figure 61. In particular, the forward motion capabilities of the rover are used to compensate the distance between the aerial platform and the inspection tool. In this figure, the error between a desired reference value of the elbow (i.e. the only joint that can push away the tool from the airframe in the forward direction) is reported along with the longitudinal position of the platform over the pipe. This task is accomplished trying to maintain the value of the joint elbow to a desired value (in our platform we tune this value at 0.5 rad). In Figure 62 the commanded position of the tool along the x -axis, the position of the platform of the pipe (i.e. the first joint of the kinematic system) and the error between the current elbow joint value and the desired one are reported.

During the manipulation, when the tool is moved in the forward direction, the battery-sliding system prevents the unbalancing of the platform towards the forward direction (i.e. the inclination around the pitch axis). The effect of the controller is depicted in Figure 62. Here, the behaviour of the platform and the estimated torque around the y -axis with and without the pitch stabilization task are reported. It is clear how the motion of the battery pack nullifies the torque acting on the platform base frame.

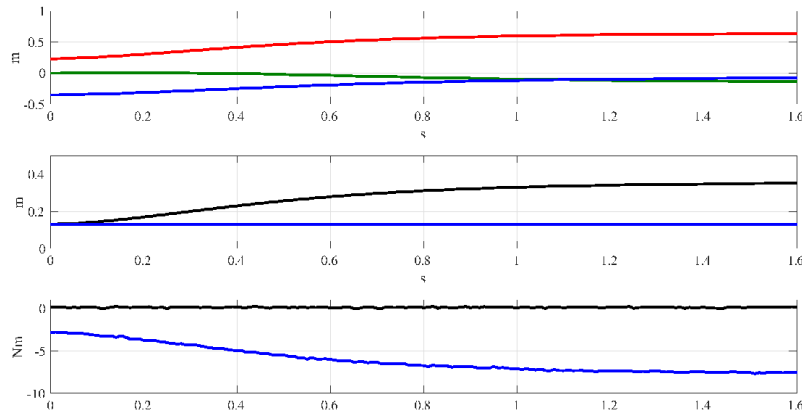


Figure 62: Compensation around the pitch axis during the motion of the arm, thanks to the battery sliding mechanism. From top to bottom, the Cartesian position of the end-effector, the position of the battery, the estimated wrench around the y axis (pitch). In blue the same data without the projection onto the null space.

The second test has been performed in a simplified mock-up to assess the overall effectiveness of the inspection system. In this context, the robot has been manually placed on a duct of 6 inches, and the arm is used to analyse the corrosion of an 8 inches pipe placed on its left side. During the manipulation, the hierarchical controller is enabled to stabilize the platform. This pipe has been intentionally damaged by scratching its internal section as shown in Figure 67. This setup is depicted in Figure 63.



Figure 63: Lateral inspection of an 8 inches pipe with EMAT sensors, in a laboratory mock-up.

In this test, a lateral inspection has been planned in order to place the tool directly on the damaged section. To reach this point, the center of gravity of the entire system slightly moves far from the center of mass of the hybrid base. This cause the unbalancing of the platform that must be compensated to prevent the slipping down of the robot from the operating position. To demonstrate the effectiveness of the hierarchical controller, we monitored the estimated torques around the pipe, namely τ_x (i.e. the torque acting around the x -axis of the robot). To test the controller, the system has been tested with and without the torque compensation. In both cases, the planned motion for the joints of the arm is illustrated in Figure 64.

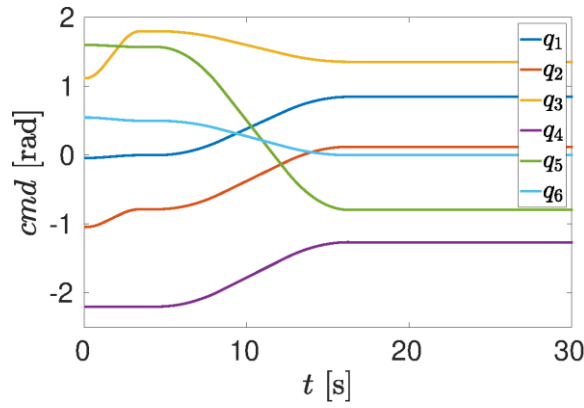


Figure 64: Time histories of joint position commands to bring the tool on the inspection point.

During the execution of this motion, the estimation of τ_x grown since the robot is unbalanced towards its left side. At the same time, to compensate for the unbalance, the deployed system controller commands the base of the robot to tilt in the opposite direction of the estimated torque. This is shown in Figure 66 (top), in which the measured rotation around the pipe (θ_m) get from the IMU sensor is reported along with the commanded one (θ_d). It is worth noticing that there is an overshooting effect in this phase that brings the robot to have a small unbalance (0.6 Nn). This is caused by the inertia of the system. However, the system remains stable on the landing point. Differently, in Figure 65 we report the same data deactivating the whole-body controller and consequently the compensation of the τ_x torque. In this case, the robot is not able to accomplish the task since it falls down from the inspection point. Figure 65 (bottom) reports how the torque grows during the motion of the tool (close to 4 Nm). Since the controller is deactivated, the desired angle with respect to the center of the pipe (θ_d) remains 0, and the torque generated by the motion of the arm caused the slipping down of the platform, in correspondence of the first dashed lines depicted in Figure 65 (top). In this test, the robot is manually handled to prevent its crash on the ground (in correspondence to the second dashed line of Figure 65(top)).

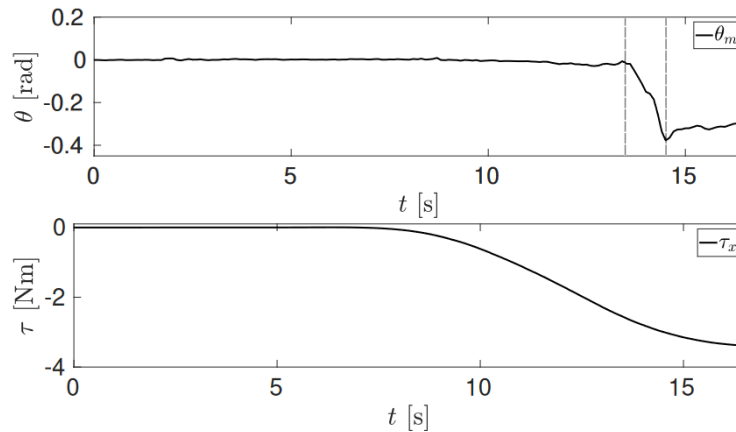


Figure 65: Measured roll angle of the platform on the pipe (top) and the estimated torque around the x axis of the pipe during the motion of the arm (bottom) without the external force compensation.

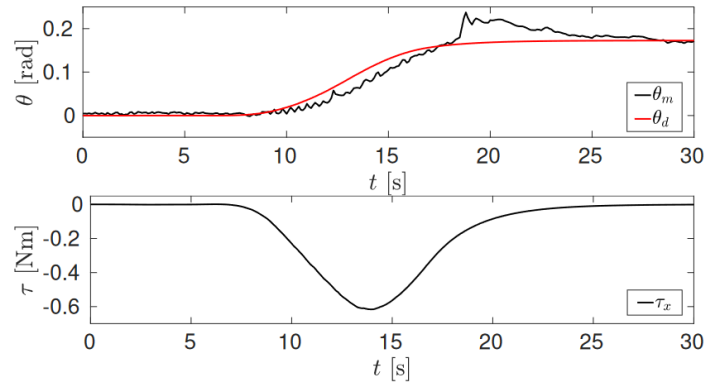


Figure 66: Measured and commanded roll angle of the platform on the pipe (top) and the estimated torque around the x axis of the pipe during the motion of the arm (bottom) with external force compensation.

As for the inspection task, we report our results in the creation of a *B-Scan* image, combining the instant thickness measurement with the rotation of the probes around the pipe. It is worth noticing that, thanks to the design of the proposed inspection tool, the creation of such a representation comes very easy, because it is directly generated as consequences of the rotation of the inspection tool around the pipe. The *B-Scan* graphic resulting from the inspection of the damaged pipe is reported in Figure 68, in which the damaged part has been detected and it is highlighted with a red rectangle. This graphic reports the wave propagation into the inspecting material. It shows the rotation of the tool around the pipe (on the *x-axis*) and the propagation time of the wave (on the *y-axis*) respectively. When the section of a material is intact (i.e. it has the same thickness), the periodicity of the waves and their amplitude over the time is similar during the tool rotation. Differently, as can be seen in the right part of the Figure 68 the wave response changes.



Figure 67: The damaged pipe used to test the inspection capabilities.

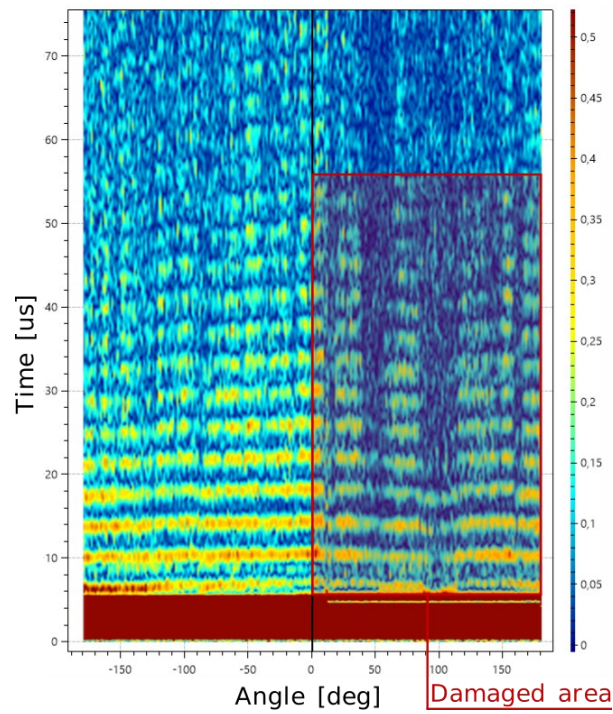


Figure 68: B-Scan graphic generated after the inspection. The rectangle marks the corroded section.

3.4. Full experiment

This section shows a sequence of images (see Figure 69) of the operation of the HRA in the outdoors mock-up scenario prepared in the context of the HYFLIERS project, executed in assisted mode.



Figure 69: Sequence of images of one of the experiments in the HYFLIERS outdoors mock-up scenario.

The experiment illustrates the different phases of the inspection flight: take-off, approaching flight, landing on the pipe, movement along the pipe using the HRA landing gear actuators while maintaining stability, stopped on the pipe for inspection while maintaining stability on the pipe, take-off from pipe, move away, approach to landing site and finally land.

4. Conclusions

This deliverable has presented several tests performed with the integrated version of the hybrid robots developed in the framework of the HYFLIERS project. They have been used to test the basic and the advanced functionalities of HYFLIERS' systems to make sure that all the subsystems and the entire robots performs work as expected. At this stage of the project, the final versions of both robots have been properly tested through extensive experimentation in a controlled scenario aiming the use case targeted by each robot. As conclusions, although there is a lot of pending work to reach industrial levels of TRLs, both systems seem to be promising solutions for their respective use cases.

These preliminary tests have been accomplished in both indoor and outdoor environments. After these tests the technology developers consider the system ready to start the validation phase and the end-user evaluation.

References

- [1] Michael Grupp. evo: Python package for the evaluation of odometry and slam. <https://github.com/MichaelGrupp/evo>, 2017.